

# The MACHO Project: Microlensing Optical Depth towards the Galactic Bulge from Difference Image Analysis

C. Alcock<sup>1,2</sup>, R.A. Allsman<sup>3</sup>, D.R. Alves<sup>4</sup>, T.S. Axelrod<sup>5</sup>, A.C. Becker<sup>6</sup>, D.P. Bennett<sup>2,7</sup>,  
K.H. Cook<sup>1,2</sup>, A.J. Drake<sup>1,5</sup>, K.C. Freeman<sup>5</sup>, M. Geha<sup>1</sup>, K. Griest<sup>2,8</sup>, M.J. Lehner<sup>9</sup>,  
S.L. Marshall<sup>1,2</sup>, D. Minniti<sup>1,10</sup>, C.A. Nelson<sup>1,2</sup>, B.A. Peterson<sup>5</sup>, P. Popowski<sup>1</sup>,  
M.R. Pratt<sup>11</sup>, P.J. Quinn<sup>12</sup>, C.W. Stubbs<sup>2,5,6</sup>, W. Sutherland<sup>13</sup>, A.B. Tomaney<sup>6</sup>,  
T. Vandehei<sup>8</sup>, AND D.L. Welch<sup>14</sup>

(The MACHO Collaboration)

---

<sup>1</sup>Lawrence Livermore National Laboratory, Livermore, CA 94550

<sup>2</sup>Center for Particle Astrophysics, University of California, Berkeley, CA 94720

<sup>3</sup>Supercomputing Facility, Australian National University, Canberra, ACT 0200, Australia

<sup>4</sup>Space Telescope Science Institute, 3700 San Martin Dr, Baltimore, MD 21218

<sup>5</sup>Research School of Astronomy and Astrophysics, Weston Creek, Canberra, ACT 2611, Australia

<sup>6</sup>Department of Astronomy and Physics, University of Washington, Seattle, WA 98195

<sup>7</sup>Department of Physics, University of Notre Dame, Notre Dame, IN 46556

<sup>8</sup>Department of Physics, University of California, San Diego, CA 92093

<sup>9</sup>Department of Physics, University of Sheffield, Sheffield S3 7RH, UK

<sup>10</sup>Departamento de Astronomia, P. Universidad Católica, Casilla 104, Santiago 22, Chile

<sup>11</sup>Center for Space Research, MIT, Cambridge, MA 02139

<sup>12</sup>European Southern Observatory, Karl Schwarzschild Str. 2, D-85748 Garching bei München, Germany

<sup>13</sup>Department of Physics, University of Oxford, Oxford OX1 3RH, UK

<sup>14</sup>Department of Physics and Astronomy, McMaster University, Hamilton, ON L8S 4M1, Canada

## ABSTRACT

We present the microlensing optical depth towards the Galactic bulge based on the detection of 99 events found in our Difference Image Analysis (DIA) survey. This analysis encompasses three years of data, covering  $\sim 17$  million stars in  $\sim 4$  deg<sup>2</sup>, to a source star baseline magnitude limit of  $V = 23$ . The DIA technique improves the quality of photometry in crowded fields, and allows us to detect more microlensing events with faint source stars. We find this method increases the number of detection events by 85% compared with the standard analysis technique. DIA light curves of the events are presented and the microlensing fit parameters are given. The total microlensing optical depth is estimated to be  $\tau_{total} = 2.43_{-0.38}^{+0.39} \times 10^{-6}$  averaged over 8 fields centered at  $l = 2^{\circ}68$  and  $b = -3^{\circ}35$ . For the bulge component we find  $\tau_{bulge} = 3.23_{-0.50}^{+0.52} \times 10^{-6}$  assuming a 25% stellar contribution from disk sources. These optical depths are in good agreement with the past determinations of the MACHO (Alcock et al. 1997a) and OGLE (Udalski et al. 1994) groups, and are higher than predicted by contemporary Galactic models. We show that our observed event timescale distribution is consistent with the distribution expected from normal mass stars, if we adopt the stellar mass function of Scalo (1986) as our lens mass function. However, we note that as there is still disagreement about the exact form of the stellar mass function, there is uncertainty in this conclusion. Based on our event timescale distribution we find no evidence for the existence of a large population of brown dwarfs in the direction of the Galactic bulge.

*Subject headings:* dark matter - Galaxy: structure - gravitational lensing - stars: low-mass

## 1. INTRODUCTION

Over the past seven years the MACHO group has been making observations of the Galactic bulge in order to determine some of the fundamental properties of our Galaxy. The Milky Way is expected to be an SAB(rs)bc or SAB(r)bc type spiral galaxy (de Vaucouleurs 1964; Fux 1997) with four spiral arms (Vallee 1995). However, very little is known about the mass distributions of the various components of our Galaxy (bulge, spheroid, disk, halo). Galactic microlensing surveys provide some insight into the structure and dynamics of the inner Galaxy, spiral arms and the halo. Unlike most types of observation, the presence of lensing objects can be detected independent of their luminosities. Microlensing is sensitive to the mass distribution rather than light, this makes microlensing a powerful way of investigating the mass density within our Galaxy. Furthermore, microlensing can be used to investigate the stellar mass function to the hydrogen burning limit, both within our Galaxy and other nearby galaxies.

The amplification of a source star during gravitational microlensing is related to the projected lens-source separation  $u$  normalised by the angular Einstein Ring radius  $R_E$ . This is given by

$$A(u) = \frac{u^2 + 2}{u\sqrt{u^2 + 4}}. \quad (1)$$

The timescale of a microlensing event,  $\hat{t}$ , is characterised by the time it takes for the Einstein ring associated with a foreground compact lensing object, to transit a background source star at velocity  $v_\perp$ . The size of the Einstein ring, for a lens with mass  $M$  (in  $M_\odot$ ), an observer-lens distance  $D_d$ , and a source-observer distance  $D_s$ , is given by

$$R_E = 2.85 \text{AU} \sqrt{\frac{MD_d(1 - \frac{D_d}{D_s})}{1 \text{kpc}}}. \quad (2)$$

The lensing timescale is  $\hat{t} \equiv 2R_E/v_\perp$ . Hence, if  $R_E$  were known, this would enable us to constrain some of the physical parameters of a microlensing event ( $M$ ,  $D_s$ ,  $D_d$ ). However,  $R_E$  is not known, generally, so it is not possible to determine the lens masses from individual microlensing events. Nevertheless, under special circumstances it is possible to impose additional constraints on these microlensing event parameters when quantities such as, the physical size of the source star (Alcock et al. 1999d) or the projected

transverse velocity of the lens (Alcock et al. 1995) are measured.

Photometry of the stars monitored by the MACHO project has previously been carried out using a fixed position PSF photometry package SoDoPhot (Son of DoPhot, Bennett et al. 1993). In 1996 we introduced a second reduction method, Difference Image Analysis (hereafter DIA). The DIA technique enables us to detect microlensing events which go undetected with the SoDoPhot photometry because the events are due to stars which are too faint to be detected when unlensed. This technique follows on from the work of Crots (1992), Phillips & Davis (1995) and Tomaney & Crots (1996), and allows us to detect and perform accurate photometry on these new microlensing events found in the reanalysis of bulge images.

Recently, the MACHO and OGLE groups reported that the microlensing optical depth towards the Galactic bulge was a factor of 2 larger than expected from stellar number density. That is, the optical depth found by OGLE is  $3.3 \pm 1.2 \times 10^{-6}$  (Udalski et al. 1994) and by MACHO is  $3.9^{+1.8}_{-1.2} \times 10^{-6}$  for 13 clump giant source star events out of a 41 event sample (Alcock et al. 1997a). It was suggested that the size of these measurements could be explained by the presence of a bar oriented along our line-of-sight to the bulge (Paczynski et al. 1994; Zhao et al. 1995). The density profile of the proposed bar is given by

$$\rho_b = \frac{M}{20.65abc} \exp\left(-\frac{w^2}{2}\right), \quad (3)$$

where

$$w^4 = \left[\left(\frac{x}{a}\right)^2 + \left(\frac{y}{b}\right)^2\right]^2 + \left(\frac{z'}{c}\right)^4. \quad (4)$$

For the bulge galactocentric coordinates ( $x, y, z'$ ):  $x = \cos \theta - \eta \cos b \cos(l - \theta)$ ,  $y = -\sin \theta - \eta \cos b \sin(l - \theta)$ ,  $z' = \eta \sin b$ . The bar inclination angle  $\theta$  is oriented in the direction of increasing  $l$ , and  $\eta = D_s/D_{8.5}$  is the ratio of the source distance relative to a galactocentric distance, taken to be 8.5 kpc. The terms  $a$ ,  $b$  and  $c$  define the bar scale lengths.

The idea that our Galaxy harbours a bar at its centre is not a new one as it was first suggested by de Vaucouleurs (1964) because of the similarity of the gas dynamics observed in our galaxy with other barred galaxies. Binney et al. (1991) provided further evidence for a bar from star counts. The DIRBE results

of Dwek et al. (1995) were also found to be consistent with this prediction. The presence of such a bar is an important way of explaining the interaction of the disk, halo and the spiral density waves in the disk.

A number of authors have adopted a bar into their Galactic models and have adopted various values of the bar orientation (Paczynski et al. 1994; Peale 1998; Zhao & Mao 1996) and bar mass (Peale 1998; Zhao & Mao 1996). Other authors have also proposed that large optical depth contributions could come from the disk component (Evans et al. 1998), or the Galactic stellar mass function (Méra, Chabrier, & Schaeffer 1998; Han & Chang 1998; Zhao & Mao 1996).

In this paper we present a new value for the microlensing optical depth and investigate what is known about the Galactic parameters with most influence the optical depth. In the next section we will detail the observational setup. In §3, we will outline the reduction procedure. We will next review the microlensing event selection process in §4. The results of our analysis are presented in §5, and we will discuss how the microlensing detection efficiency was calculated in §6. The microlensing optical depth for the sample of fields presently analysed with DIA and for each of the individual field will be presented in §7. In §8, we will review what is known about the most important factors affecting the observed optical depth and discuss the implications of our results. In the final section we summarise the results of this work.

## 2. OBSERVATIONS

The MACHO observation database contains over 90000 individual observations of the Galactic bulge and Magellanic Clouds. The Galactic bulge dataset consists of  $\sim 30000$  observations of  $94, 43' \times 43'$  fields. The largest set of microlensing events reported to date was given by Alcock et al. (1997b). This consisted of 41 events detected from one year of observations in 28 of those Galactic bulge fields. The observations in this work were taken between March 1995 and August 1997. We consider  $\sim 3000$  Galactic bulge observations from eight fields. The central location of the eight fields is  $l = 2^\circ 68, b = -3^\circ 35$ .

All observations were taken with the Mount Stromlo and Siding Spring Observatories' 1.3m Great Melbourne Telescope with the dual-colour wide-field *Macho camera*. The Macho camera consists of two sets of four CCDs, one for red band ( $R_M$ ) images, and the other for blue band ( $B_M$ ) images. These observations

were taken simultaneously by employing a dichroic beam splitter. Each CCD is 2k by 2k with an on-the-sky pixel size of  $0.63''$ . All bulge observations used 150 second exposures.

The median seeing of the data subset is  $\sim 2.1''$  and the median sky levels are  $B_M \sim 1300$  ADU and  $R_M \sim 2200$  ADU. To improve the average data quality of our light curves we have chosen to reject  $\sim 350$  observations where the seeing of the observation was  $> 4''$  or  $B_M$  band sky level was  $> 8000$  ADU. The number of observations for each field varies. The smallest number of observations in this subset is 204 for field 159 and the largest is 334 for field 104. Low Galactic latitude fields such as field 104 have a higher observing priority than, for example field 159, because the microlensing optical depth is expected to be higher closer to the Galactic center.

## 3. REDUCTION TECHNIQUE

The DIA technique involves matching a good seeing *reference* image to other images of the same field, so called *test* images. The test images are first spatially registered to the reference images and the PSFs of the images are matched. The test images are then photometrically normalised (flux matched) to the reference image and the images are differenced to reveal variable stars, asteroids, novae, etc. These variables and microlensing events are searched for in each difference frame and photometry is performed on the entire set of difference images (see Alcock et al. 1999b). Initial results of our Galactic bulge DIA were presented for a single field in Alcock et al. (1999c, 1999b). In this analysis we combine that data with images from seven additional fields to determine an accurate value for the microlensing optical depth towards the Galactic bulge.

Our implementation of the DIA technique closely follows that given in Alcock et al. (1999b). In short, this involves the initial selection of 200 – 300 bright “PSF” stars from the Macho star database. The centroids of these stars are coordinate-matched in the reference and test images. The coordinate transform between the observations is calculated and used to spatially register the test observation to the reference image. The PSF stars are “cleaned” of neighbouring stars and then combined to provide a high signal-to-noise ratio (hereafter S/N) PSF for each observation. Next, the image matching convolution kernel is calculated from the Fourier Transforms of the two

PSFs employing the IRAF task PSFmatch. The reference image is convolved with the empirical kernel to seeing-match the images. The fluxes in the two observations are matched to account for variances in the atmospheric extinction, and differences in the observed sky level of the two images. Lastly a difference image is formed by subtracting one of these images from the other. An object detection algorithm is applied to the images with a three  $\sigma$  threshold, in both  $R_M$ -band and  $B_M$ -band difference images. The coordinates of objects found within each passband are matched to sort the real sources from spurious ones, such as cosmic rays and noise spikes. The systematic noise is determined from the residuals of the PSF stars in each difference image. The photon noise is calculated from the test images and the PSF-matched reference image. For further detail the reader is referred to Alcock et al. (1999b) (see also Alard & Lupton 1998; Alard 1999 for similar type of difference image technique).

### 3.1. Photometry

The MACHO project has focussed on the detection of gravitational microlensing events by repeatedly imaging millions of stars in the Galaxy. The search for microlensing events has provided a consistent set of photometry for these stars spanning the duration of the experiment. This data is thus also extremely valuable for studying the properties of the stellar populations present.

In this analysis of difference images, aperture photometry is performed on all the objects detected in the difference images. For each field this aperture photometry database consisted of  $\sim 40000$  objects. As all images of each field were registered and matched to a single reference image, the centroid coordinates for each photometry measurement are the same in each image. No extinction corrections are needed as image fluxes are also matched in the DIA process. With DIA we are in the unique situation of being able to perform aperture photometry in a field which is usually very crowded with non-variable stars. All these constant sources were removed, leaving behind only the residual noise and the variations from the relatively small number of variable stars and other transient phenomena, such as microlensing events (Alcock et al. 1999b, 1999c).

At present the photometry data is put into a simple ASCII database since there are relatively few variable objects in each field relative to the total number

of stars ( $\sim 4e4/1e6$ ). In Figure 1 we present an example of the photometry for one of the microlensing events<sup>15</sup>. The oscillations in the SoDoPhot photometry light curve are due to the offset between the nearest SoDoPhot object centroid and the centroid of the microlensing source star. Changes in the seeing can cause varying amounts of flux to be sequestered into the nearest SoDoPhot PSF. The SoDoPhot centroid is fixed in position, whereas DIA uses the actual event's centroid.

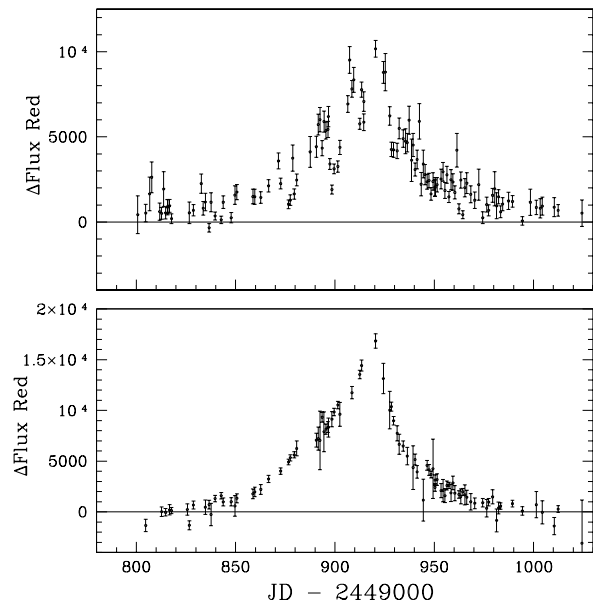


Fig. 1.— Red bandpass difference flux light curves for one of the exotic microlensing events detected in this analysis. Top: baseline subtracted SoDoPhot (PSF) photometry. Bottom: DIA aperture photometry.

## 4. EVENT SELECTION

There are a number of well known theoretical properties of microlensing which can be used to select events. That is to say, the light curves of stars affected by microlensing should exhibit: a single, symmetric, achromatic excursion from a flat baseline. In reality these properties serve only as a guide, since there are a number of exceptions to each of them (see Drake 2000). For instance, the amplification may not be

<sup>15</sup>The asymmetry is most likely due to either binary lensing or parallax. A similar microlensing event was presented in Alcock et al. (1999d).

achromatic when various types of blending are considered (Alcock et al. 1999b). Multiple peaks can, and do occur for many types of exotic microlensing events, such as binary lensing and binary source events. Furthermore, all microlensing events are affected to some degree by the parallax induced by the Earth’s orbital motion around the Sun. In most cases this is negligible, but in some circumstances the magnified peak shows a significant asymmetry (see Alcock et al. 1995). Therefore, a more rigorous set of selection criteria is necessary.

In our DIA microlensing event selection process we firstly required that the events had a total S/N > 10, in three or more photometry measurements bracketing the maximum amplification, in each band-pass. We selected only those light curves exhibiting a positive excursion from the baseline flux<sup>16</sup>. An initial estimate of the baseline flux level was determined from the median flux,  $F_{med}$ , of the difference flux light curve. In addition to these criteria, we required that each light curve passed a set of level-1.0 criteria presented in Table 1. These level-1.0 “cuts” use the flux values  $F_i$ , and uncertainties  $\sigma_i$ , measured at time  $t_i$ , to discern whether a light curve is following a microlensing-like profile, or a more variable-like curve. These initial cuts are targeted at removing particular types of variables from the event candidate list based on the general characteristics of a variable type.

In the level-1.0 selection, one cut is aimed at removing variables by the nature that they repeat. A cut on the existence of a second peak is an efficient way of removing variables from a candidate list. However, this also can have the negative effect of removing binary lensing events. For this reason we apply only a loose cut on the occurrence of a second deviation from baseline. This cut can only remove binary events with high S/N and a long duration between caustic crossings (> 110 days). The standard of the light curve photometry was also accessed in this level-1.0 selection. These level-1.0 cuts remove the high S/N variable stars from the candidate lensing event list, but a number of the lower S/N variables remained, so further cuts were necessary.

The DIA source light curves passing level-1.0 cuts were then fed through a stricter set of level-1.5 cuts. These cuts remove lower S/N variables and are based on the microlensing goodness-of-fit statistic  $\chi_m^2$ , and a constant baseline goodness-of-fit statistic  $\chi_c^2$  (per-

formed in the region  $t_{max} \pm 2t$ ). Here,  $\chi_m^2$  and  $\chi_c^2$  denote reduced chi-squared statistics. To give weight to higher S/N events we enforced what we call an  $\Omega\chi^2$  cut, this was defined as  $\Omega\chi^2 = 1000/pf \times (\chi_c^2 + \chi_m^2)$ . The symbol  $pf$  refers to the flux at peak amplification. For all light curves we required  $\Omega\chi^2 < 3.6$ .

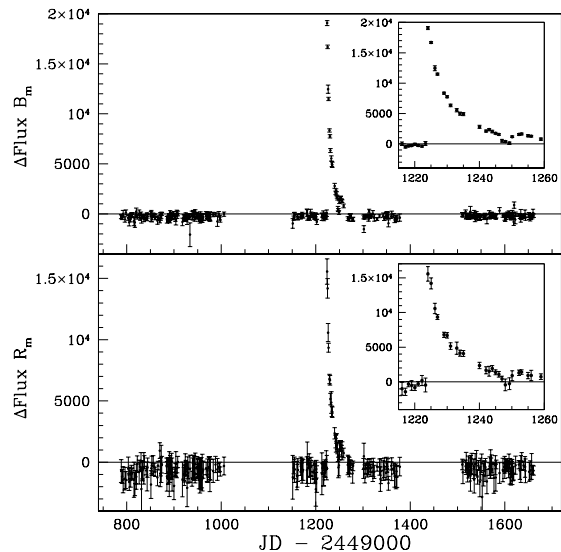


Fig. 2.— An example of a DIA light curve for one of the dwarf novae removed by our colour and fit microlensing cuts. For this event  $V - R \sim 0$ . Inset is a blow up of the outburst event.

During our analysis we found that the DIA technique was very sensitive to the detection of dwarf novae. Most of these variables can be rejected during event selection based on their poor microlensing fits. An example of these dwarf novae is presented in Figure 2. However, some faint dwarf novae light curves have large uncertainties and can thus pass a microlensing fit  $\chi^2$  cut. Because of this, we found it necessary to impose a colour cut  $(V - R)_{108} > 0.55$  and a  $V$ -magnitude cut for  $V > 17$ .  $(V - R)_{108}$  denotes the colour an event would have if seen at the average reddening of field 108 ( $E(V - R) = 0.51$ ). To determine this we have made use of the reddening values given in Alcock et al. (1998). Transformations from our  $B_M$  and  $R_M$  colours to *Cousins*  $V$  and  $R$  are given in Alcock et al. (1999a). We note that, although the colours of the dwarf novae companion stars can vary, the difference flux colour is the hue of the outburst flux component. These outburst fluxes

<sup>16</sup>The baseline itself can be negative.

appear to generally be bluer than  $V - R = 0.55$ . This colour cut removes very few stars potential sources of microlensing events since the stars observed on the blue side of  $V - R = 0.55$  are generally brighter than  $V = 17$ . In this analysis we do not apply any colour cut on the red stars in the CMD where a large number of variables stars are known to lie.

Within the analysed observations there are a number of spurious detections due to satellite trails and other transient objects. These trails generally cause multiple object detections within a given observation. We remove these spurious objects by requiring that the time of peak flux  $t_{max}$  for a microlensing event  $i$ , in image section  $j$ , does not occur at the same time as another event  $k$ , in the same image section ( $t_{max_{ij}} \neq t_{max_{kj}}$ ). The probability that two microlensing events will occur with the same value of  $t_{max}$  in close proximity, is very small. This cut also removes any spurious detections due to systematic effects which can occur when the seeing in an image is poor, or the telescope slips during an exposure.

Long timescale events are subject to significant parallax effects. To determine the efficiency of detecting such events we would have to a priori assume a distribution of sources and lenses towards the Galactic bulge. Therefore, in this analysis we impose an upper-limit on  $\hat{t}$  of one year. Similar restrictions are true for binary lensing events since the distribution of parameters for binaries is not well known. However, we think our selection should not be significantly biased against these events as our final selection contains all the events we believed were binaries in the loose level-1.0 cuts.

To summarise our level-1.5 cuts, all events must meet the following criteria:  $V - R > 0.55$ ,  $A > 1.34$ ,  $\Omega\chi^2 < 3.6$ ,  $\hat{t} < 365$  days,  $t_{max_{ij}} \neq t_{max_{kj}}$ ,  $\chi_c^2 < 30$ , plus one level-1.5 cut which is based on the event’s microlensing fit peak-flux in the  $R_M$ -band<sup>17</sup>,  $F_{pr}$ , from Table 2.

The last set of selection cuts are the level-2.0 cuts. These cuts are designed to remove the low S/N variables which are well fitted by microlensing light curves, but are nevertheless obviously variable by eye. For final selection the candidate microlensing event must pass all the level-2.0 cuts where its peak flux ( $F_{pr}$ ) is in the range of the cut. The level-2.0 cuts are also specified in Table 2. To quantify the effect of our

cuts let us mention that there were  $\sim 300000$  variable objects detected in the eight fields, only 776 of these passed our level-1.0 selection. 219 then passed the level-1.5 cuts and 99 passed the final event selection cuts (level-2.0).

We note that it is possible to express these level-1.5 and level-2.0 cuts in a more direct form. However, the procedure presented here reflects the real selection process which is progressive and most easily accomplished in stages. Furthermore, the selection of final microlensing event candidates this way is necessary in order to quantify the detection efficiency of the analysis system. The experimental determination of the microlensing optical depth requires that this detection efficiency is known. Some microlensing groups still select final candidates by eye, for instance, see Aubourg & Palanque-Delabrouille (1999).

## 5. RESULTS

We have discovered 99 microlensing event candidates. The light curves and microlensing fits for 83 events are presented in Figure 3. The actual amplification of each event was obtained by fitting the light curves with the baseline source flux as an additional parameter. The other 16 events in field 108 were shown in Alcock et al. (1999c). In each of these figures only a single season of data for each light curves is displayed. However, all the DIA light curves span three observing seasons.

The numbers of events detected in each field are given in Table 3, along with results from the SoDoPhot analysis of the same images. The coordinates and labels used for identifying the events in the datasets are given in Table 4. We will refer to events primarily using their microlensing event “alert” ID<sup>18</sup>. Each alert ID includes the year, observation target (BLG, LMC or SMC), and the order of the detection. For example, the first alert event detected in the bulge in 1995 is labeled 95-BLG-1. Microlensing events which were detected by DIA, but not in the alerts or SoDoPhot re-analysis, have a “d” before the event number (e.g. 95-BLG-d1). Events which were not found as alerts, but were detected in the subsequent analysis of SoDoPhot photometry, are labeled with an “s” (e.g. 95-BLG-s1).

<sup>17</sup>The light curves have higher S/N in the  $R_M$  band since  $B_M - R_M > 0$  in general.

<sup>18</sup>The details of microlensing alerts can be found at <http://darkstar.astro.washington.edu/>

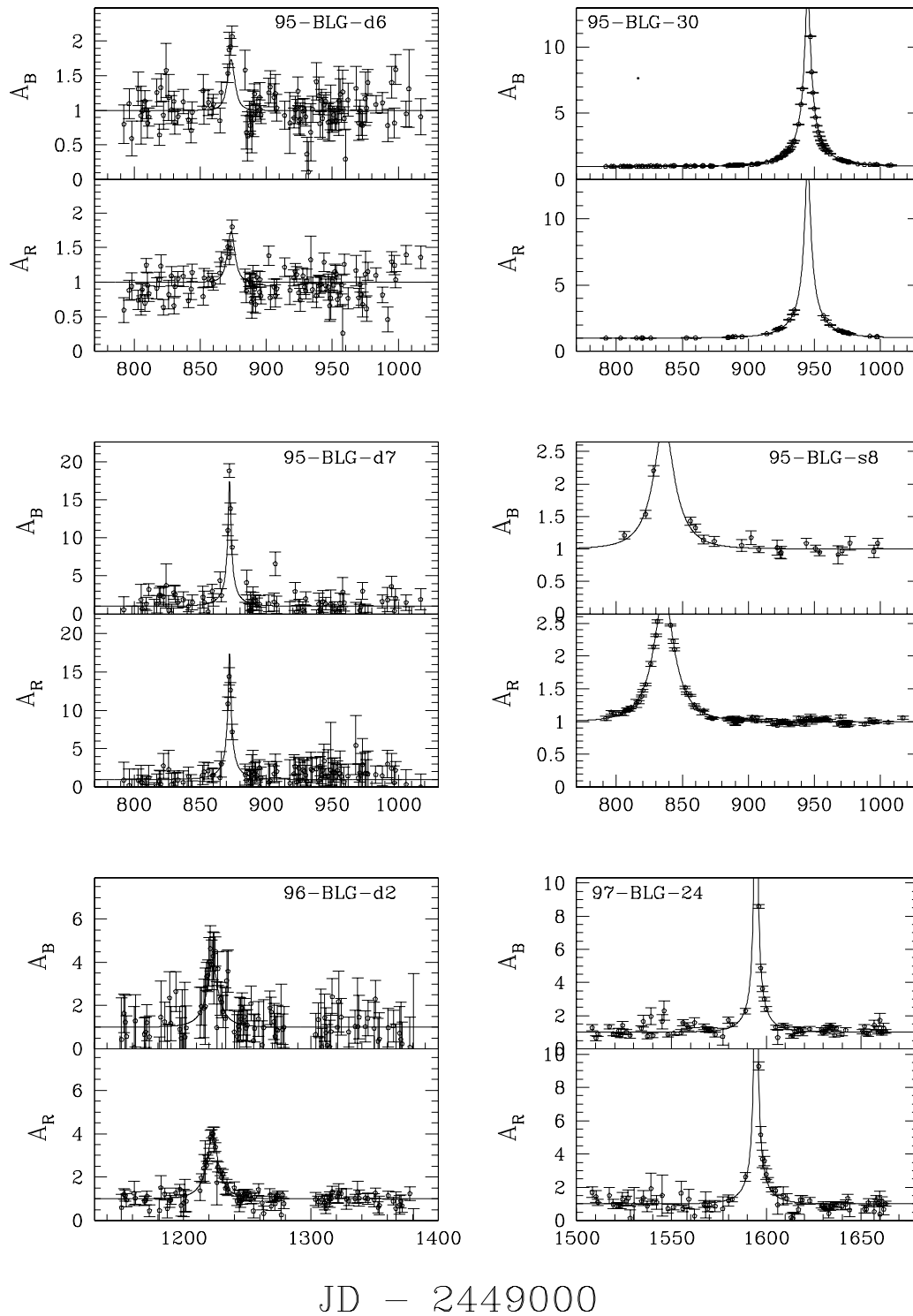


Fig. 3.— Events from Field 101. New DIA events have Ids containing “d”. New events selected with this analysis and a reanalysis of the SoDoPhot data have Ids containing “s”.



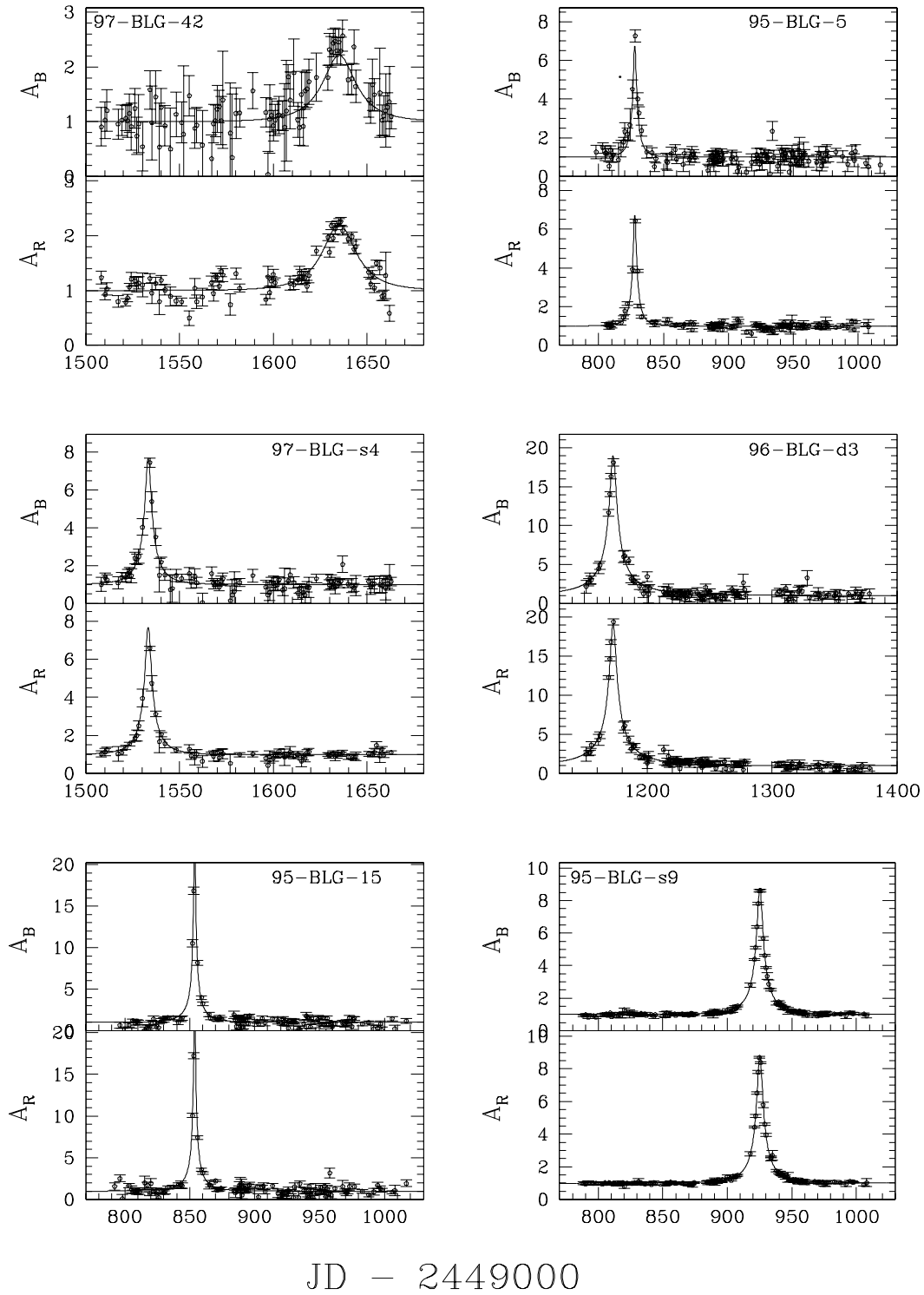


Fig. 3.— Events from Fields 101 & 104. New DIA events have Ids containing “d”. New events selected with this analysis and a reanalysis of the SoDoPhot data have Ids containing “s”.

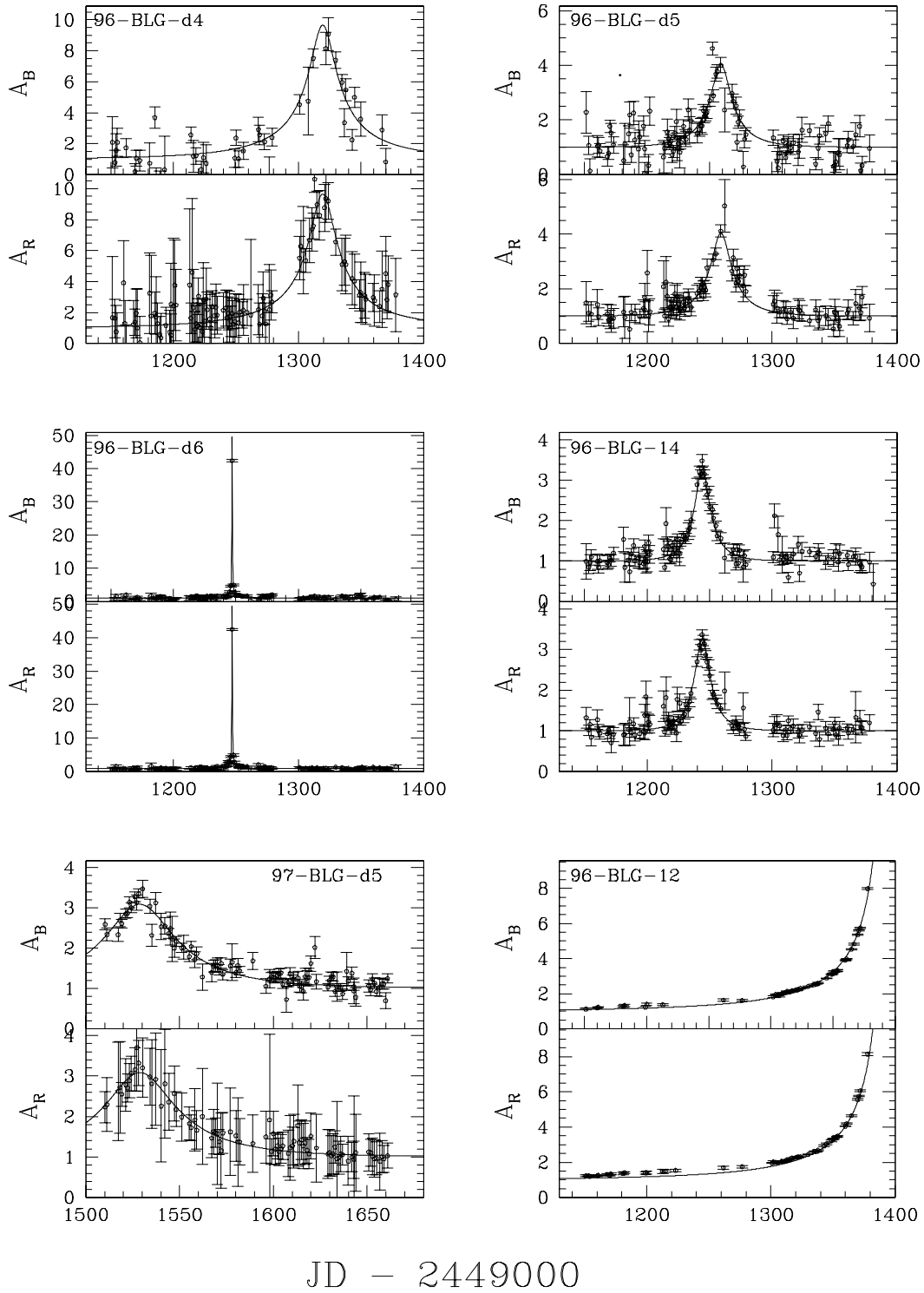


Fig. 3.— Events from Field 104. New DIA events have Ids containing “d”. New events selected with this analysis and a reanalysis of the SoDoPhot data have Ids containing “s”.

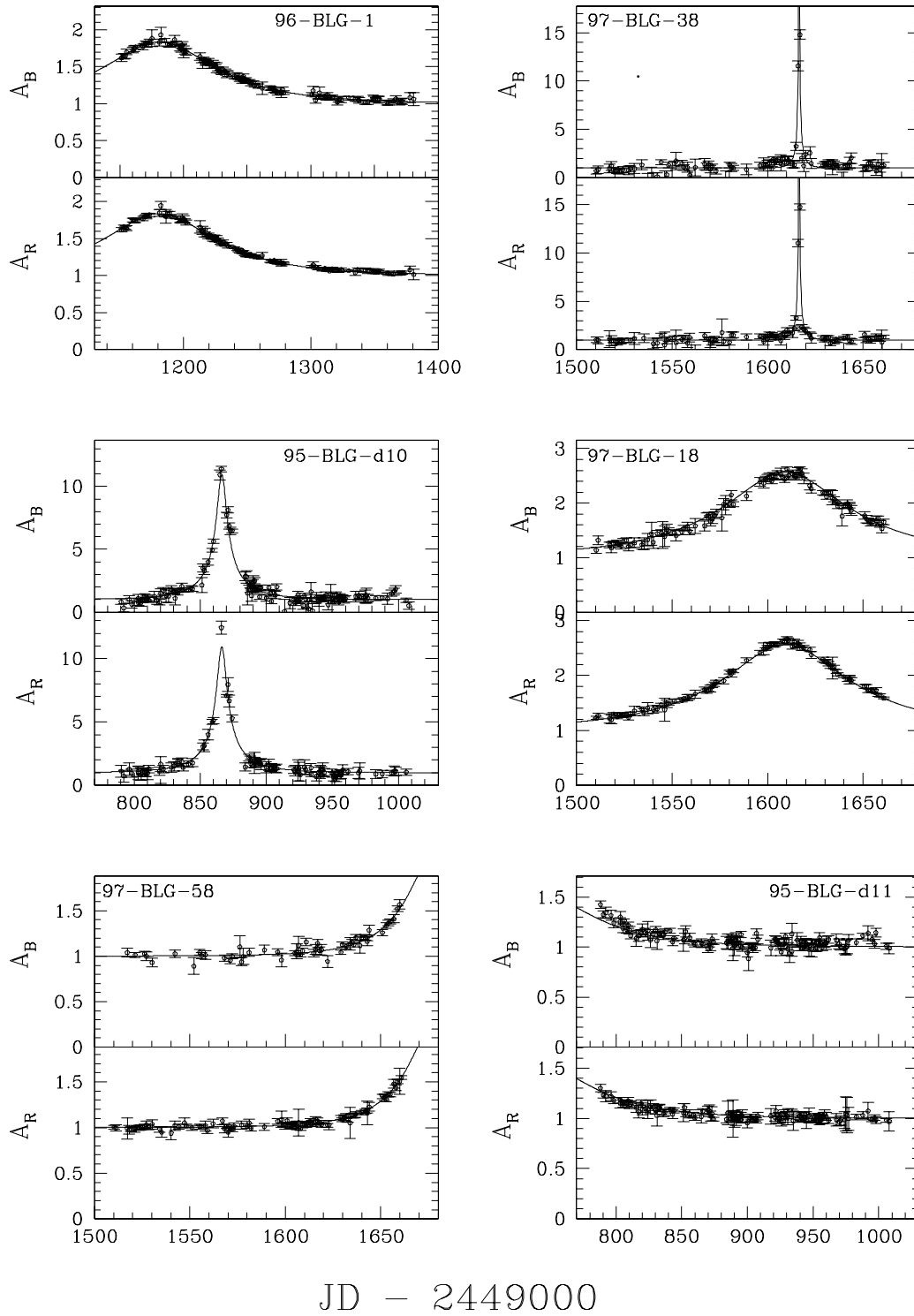


Fig. 3.— Events from Field 104 cont. New DIA events are have Ids containing “d”. New events selected with this analysis and a reanalysis of the SoDoPhot data have Ids containing “s”.

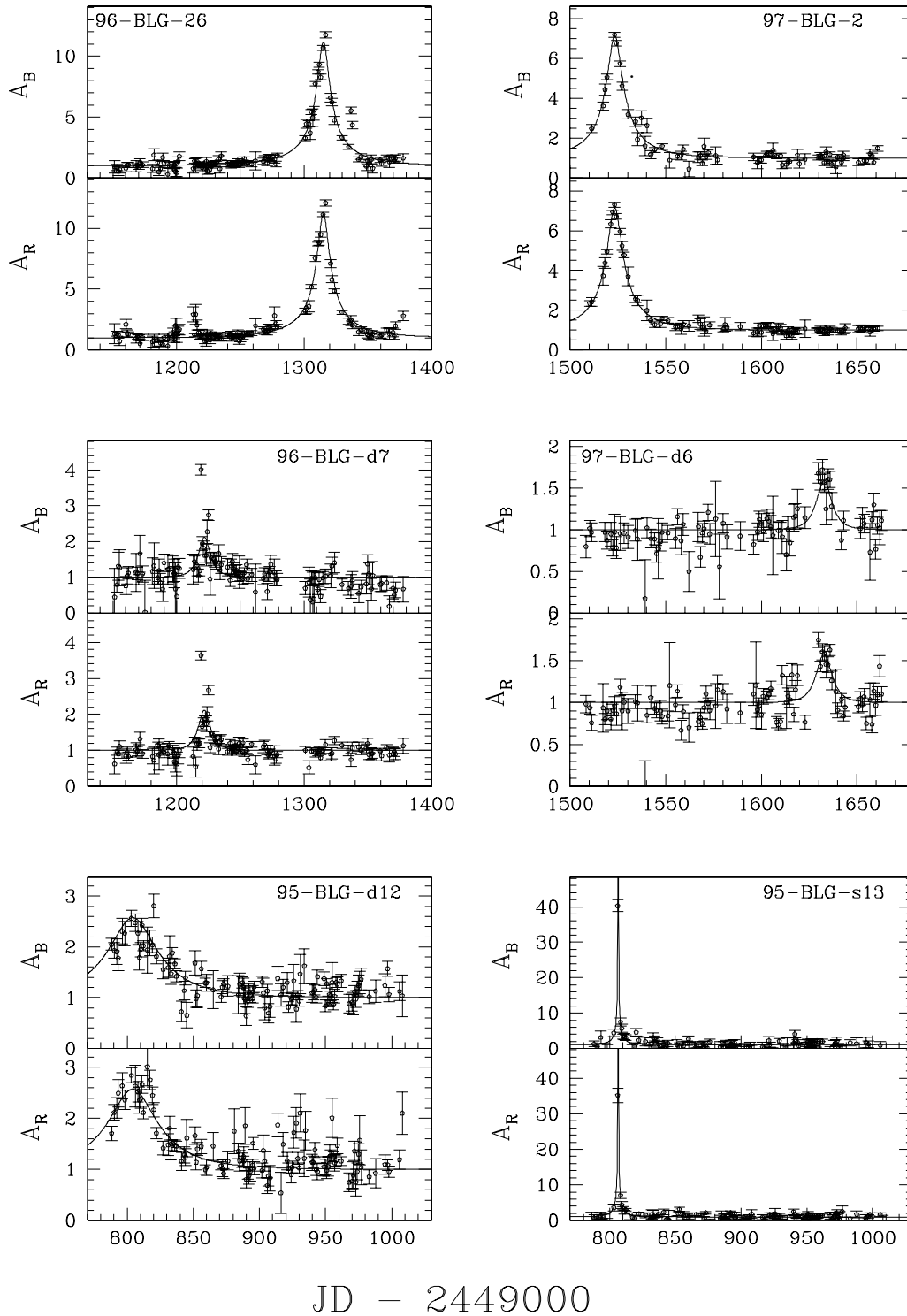


Fig. 3.— Events from Fields 104 & 113. New DIA events have Ids containing “d”. New events selected with this analysis and a reanalysis of the SoDoPhot data have Ids containing “s”.

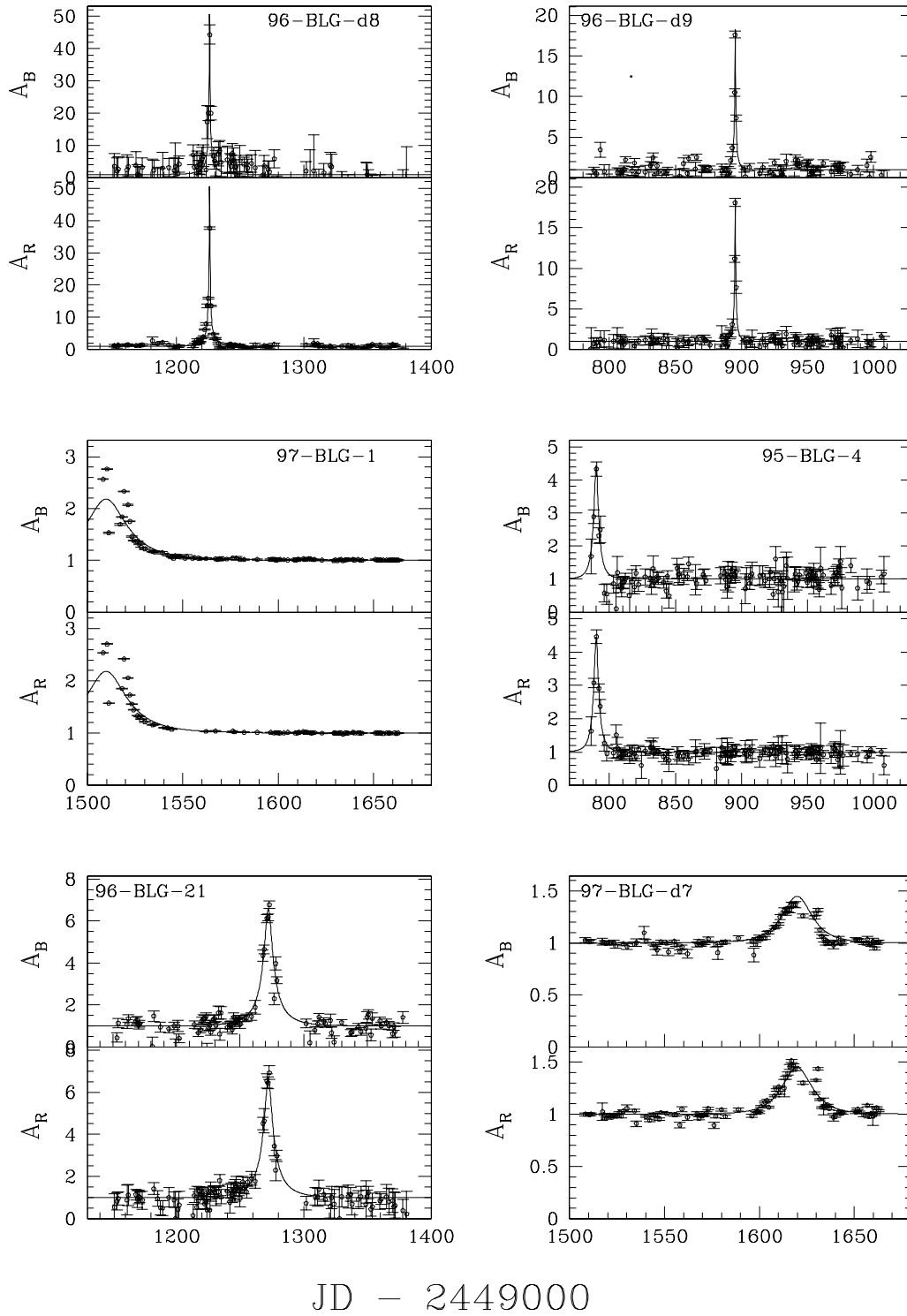


Fig. 3.— Events from Field 113. New DIA events have Ids containing “d”. New events selected with this analysis and a reanalysis of the SoDoPhot data have Ids containing “s”.

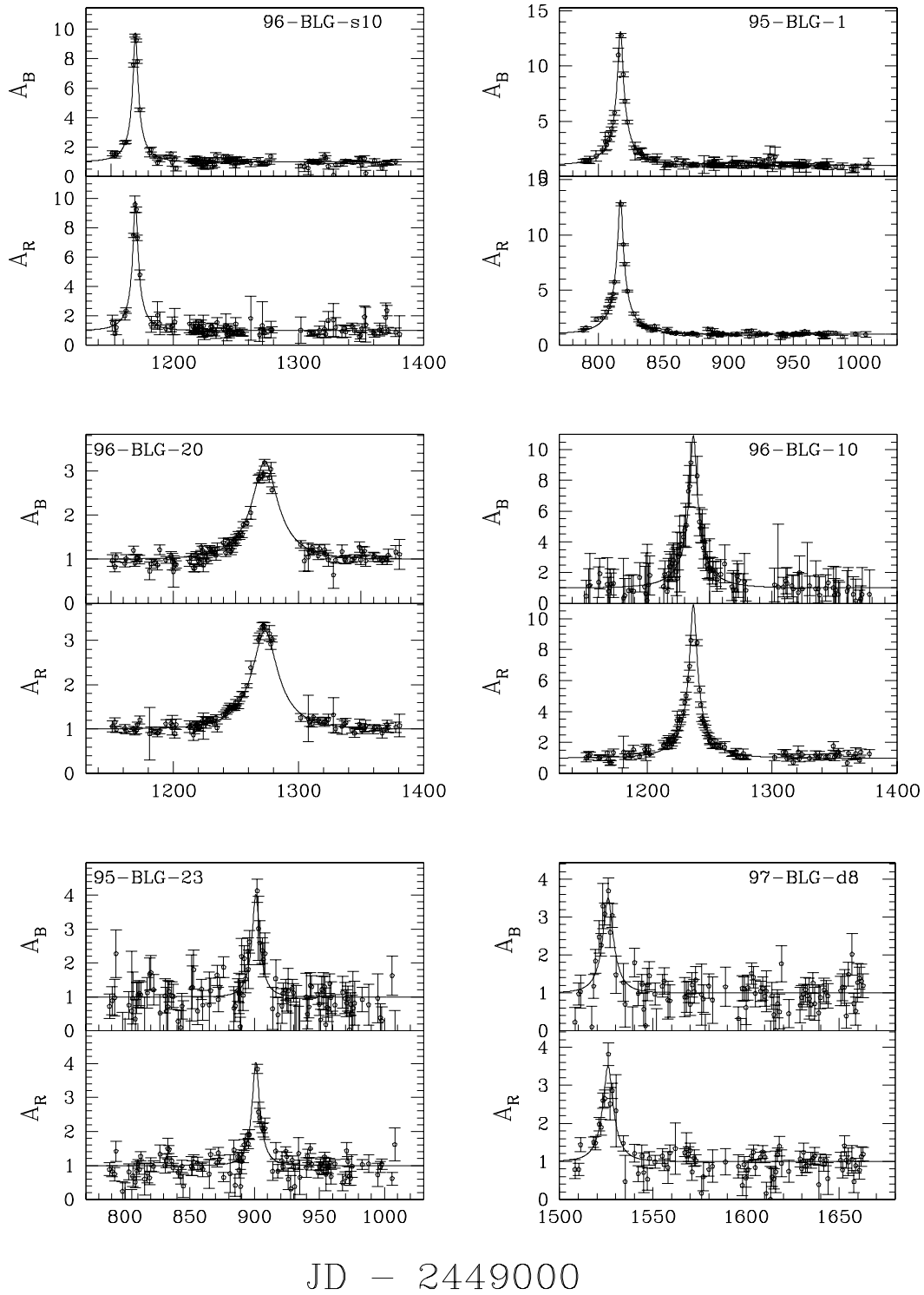


Fig. 3.— Events from Field 113 cont. New DIA events have Ids containing “d”. New events selected with this analysis and a reanalysis of the SoDoPhot data have Ids containing “s”.

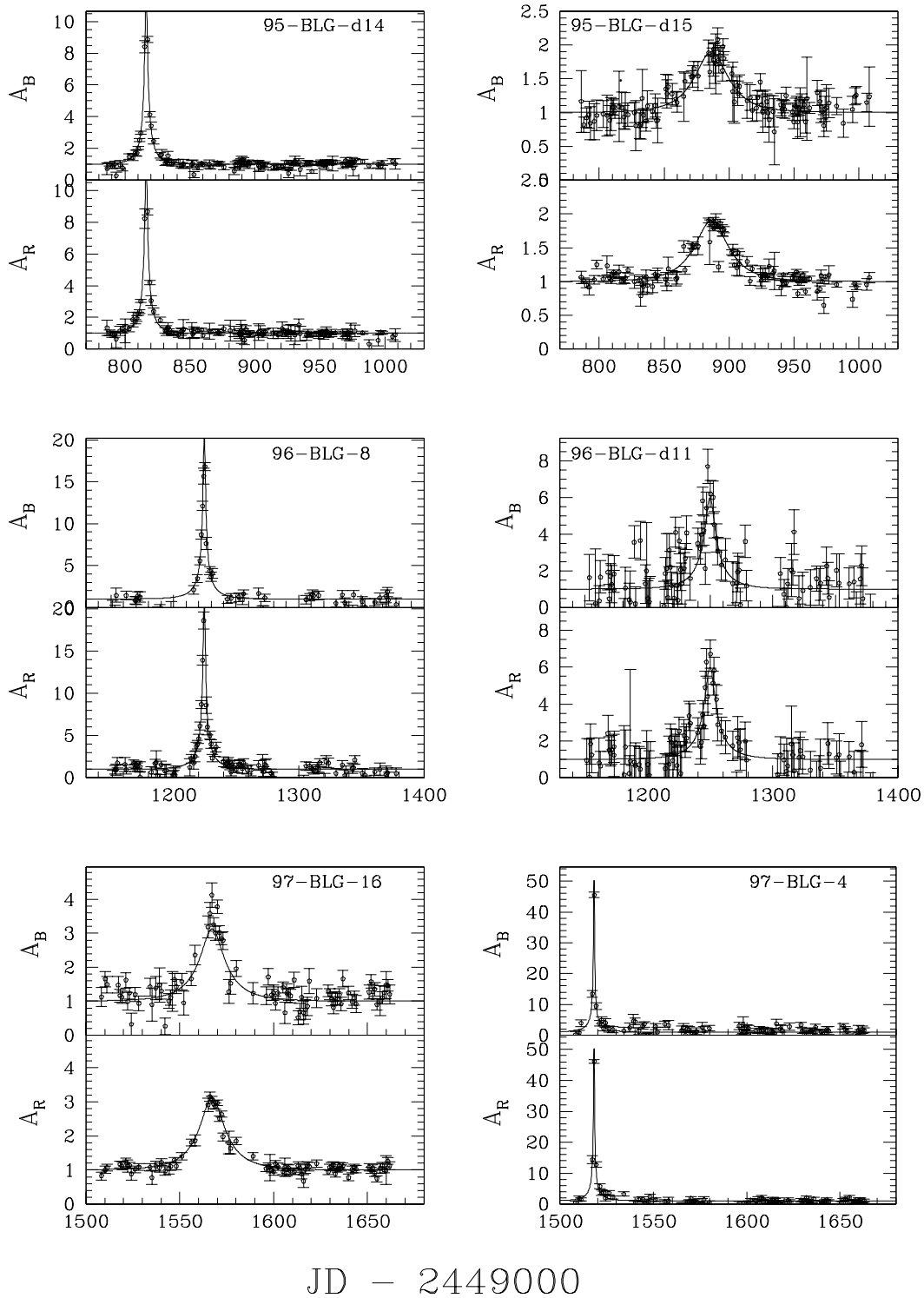


Fig. 3.— Events from Fields 113 & 118. New DIA events have Ids containing “d”. New events selected with this analysis and a reanalysis of the SoDoPhot data have Ids containing “s”.

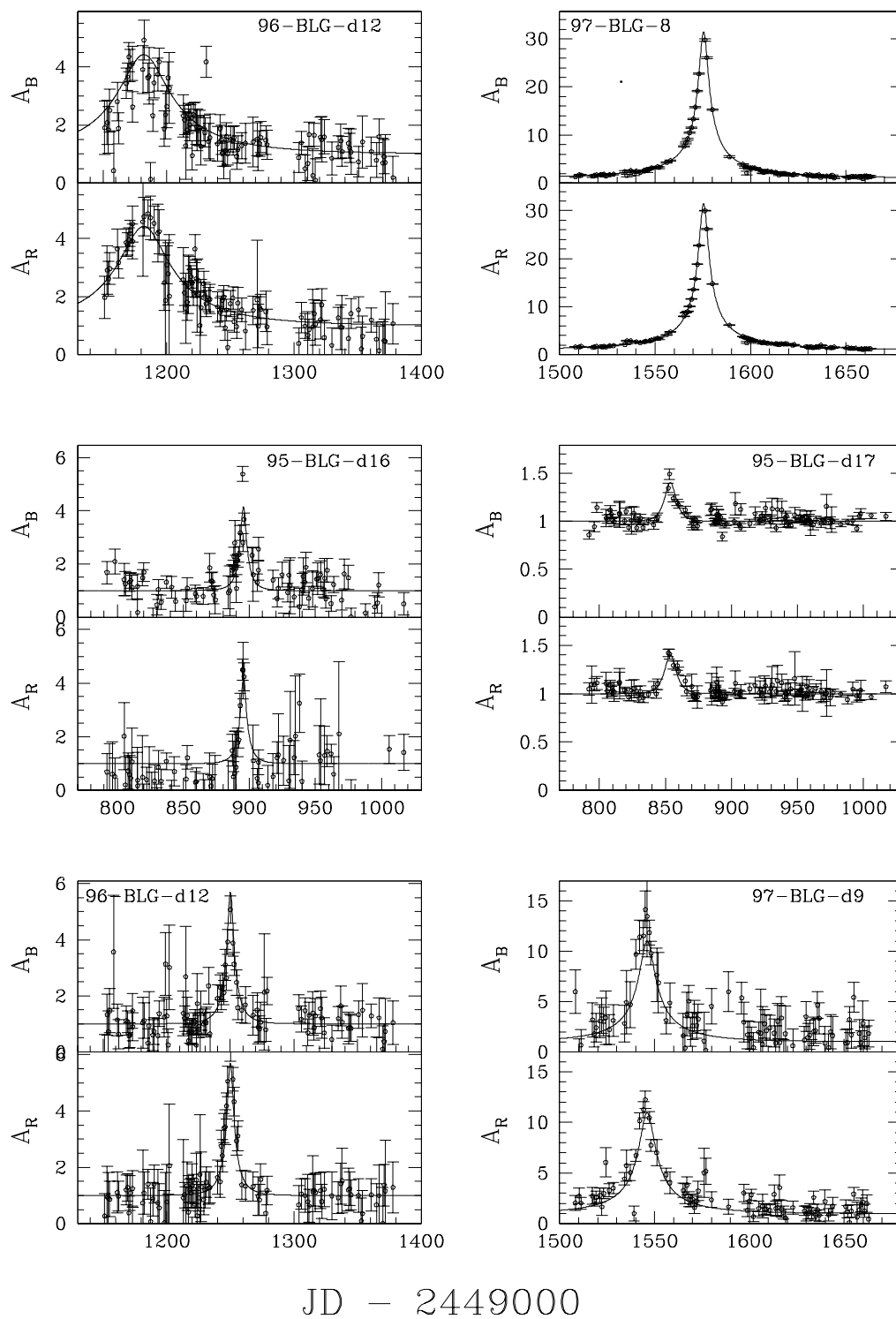
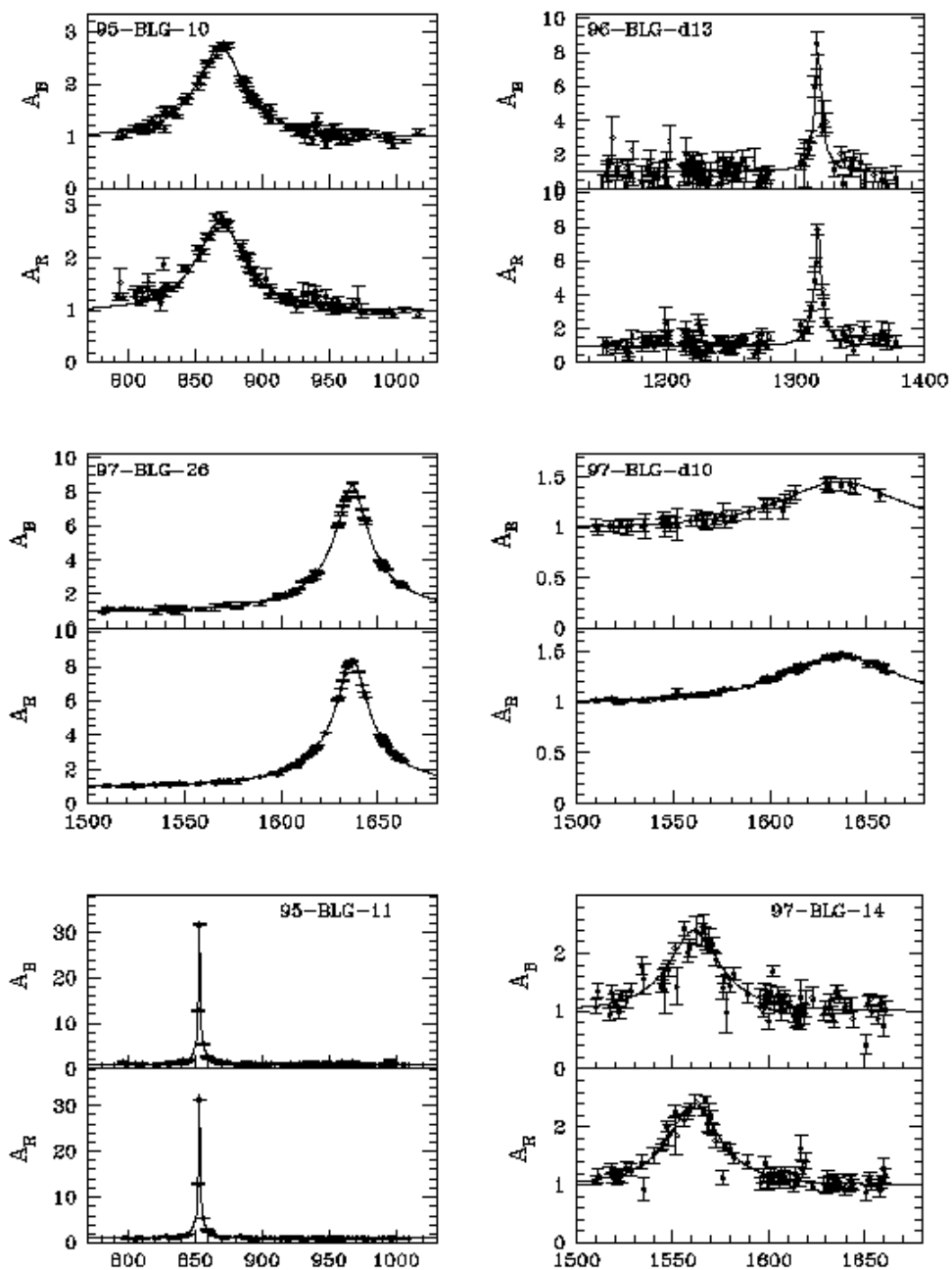


Fig. 3.— Events from Field 118. New DIA events have Ids containing “d”. New events selected with this analysis and a reanalysis of the SoDoPhot data have Ids containing “s”.





JD - 2449000

Fig. 3.— Events from Fields 118 & 119. New DIA events have Ids containing “d”. New events selected with this analysis and a reanalysis of the SoDoPhot data have Ids containing “s”.

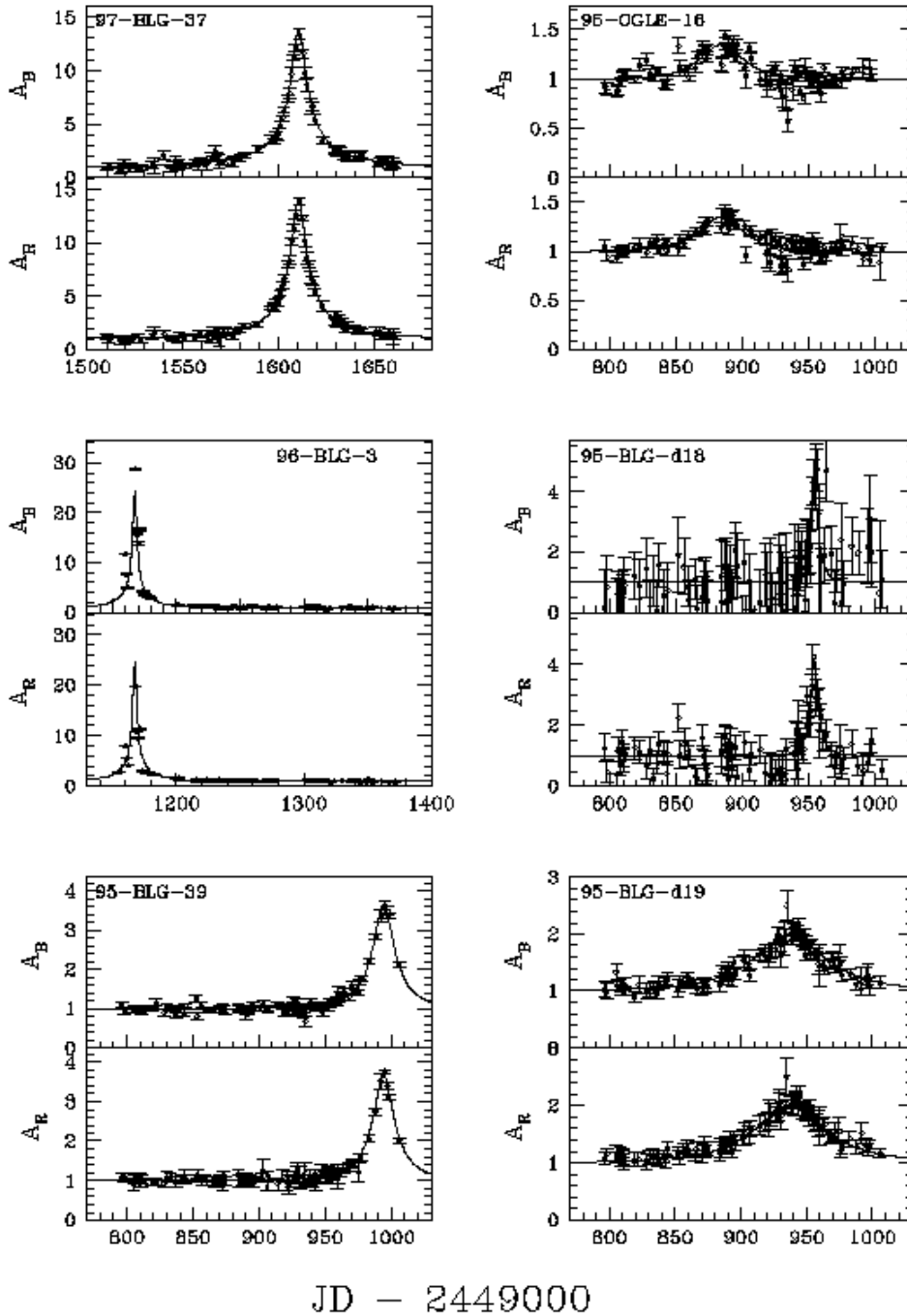


Fig. 3.— Field 119 events. New DIA events have Ids containing “d”. New events selected with this analysis and a reanalysis of the SoDoPhot data have Ids containing “s”.

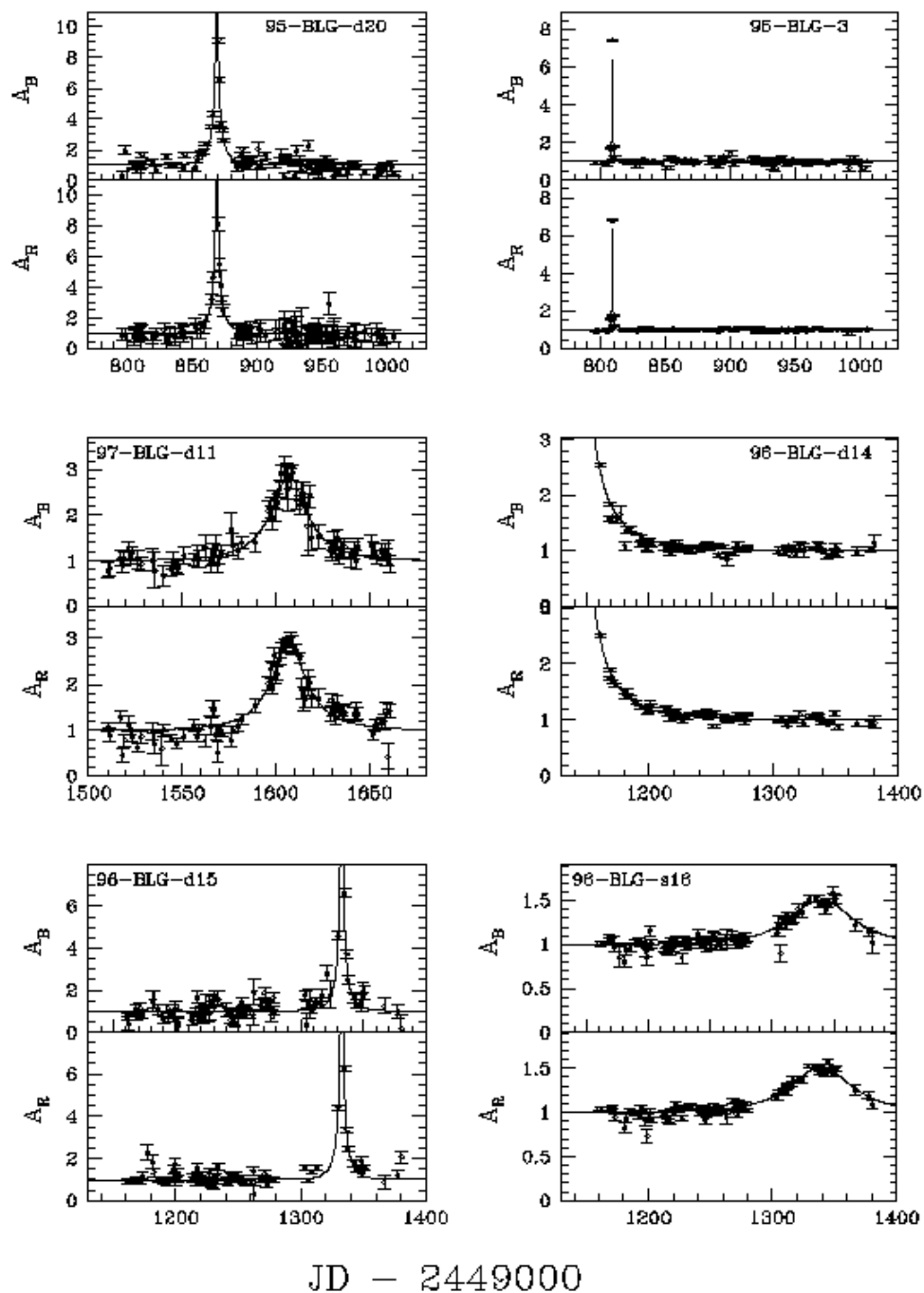


Fig. 3.— Events from Fields 119 & 128. New DIA events have Ids containing “d”. New events selected with this analysis and a reanalysis of the SoDoPhot data have Ids containing “s”.

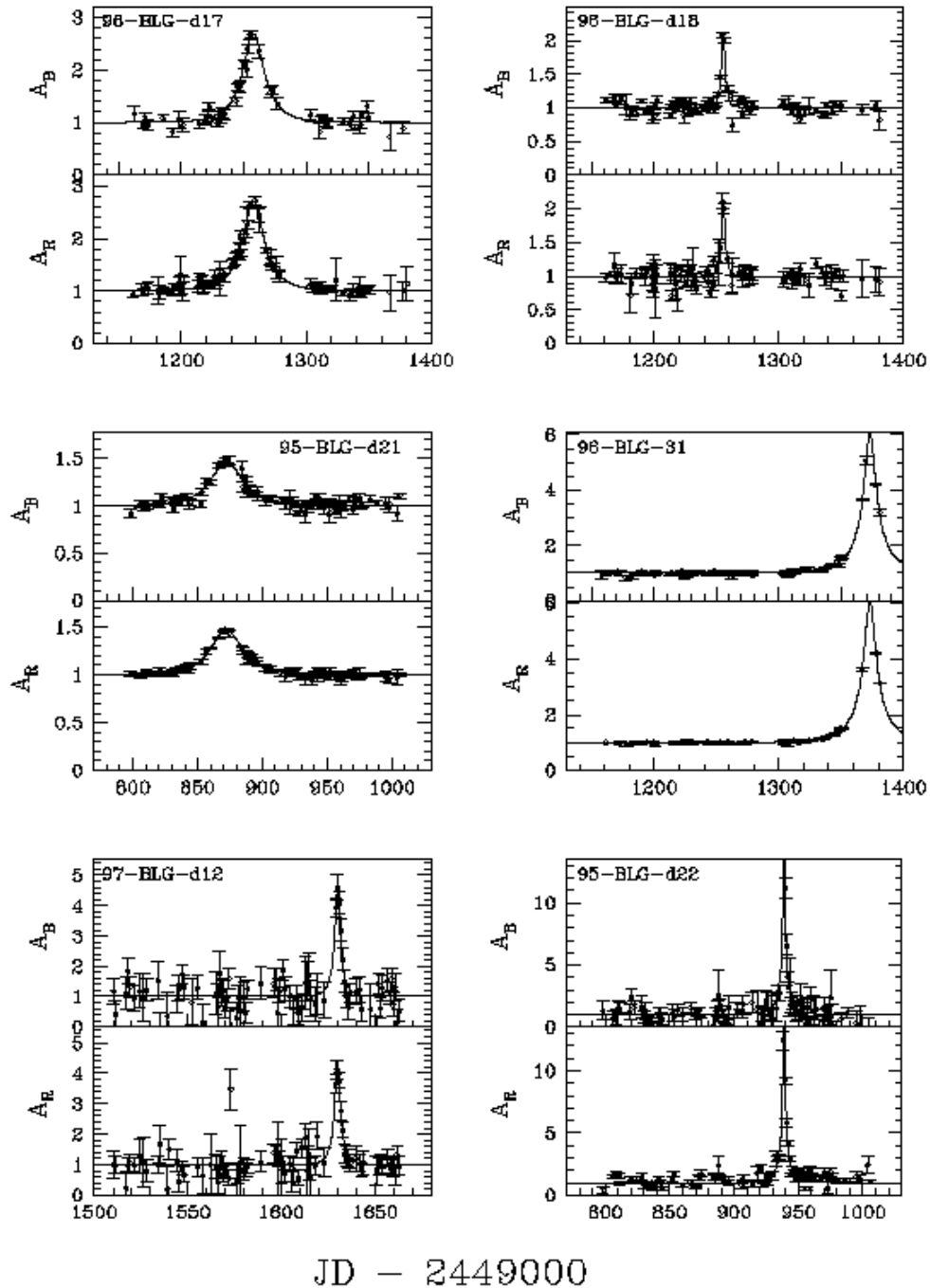
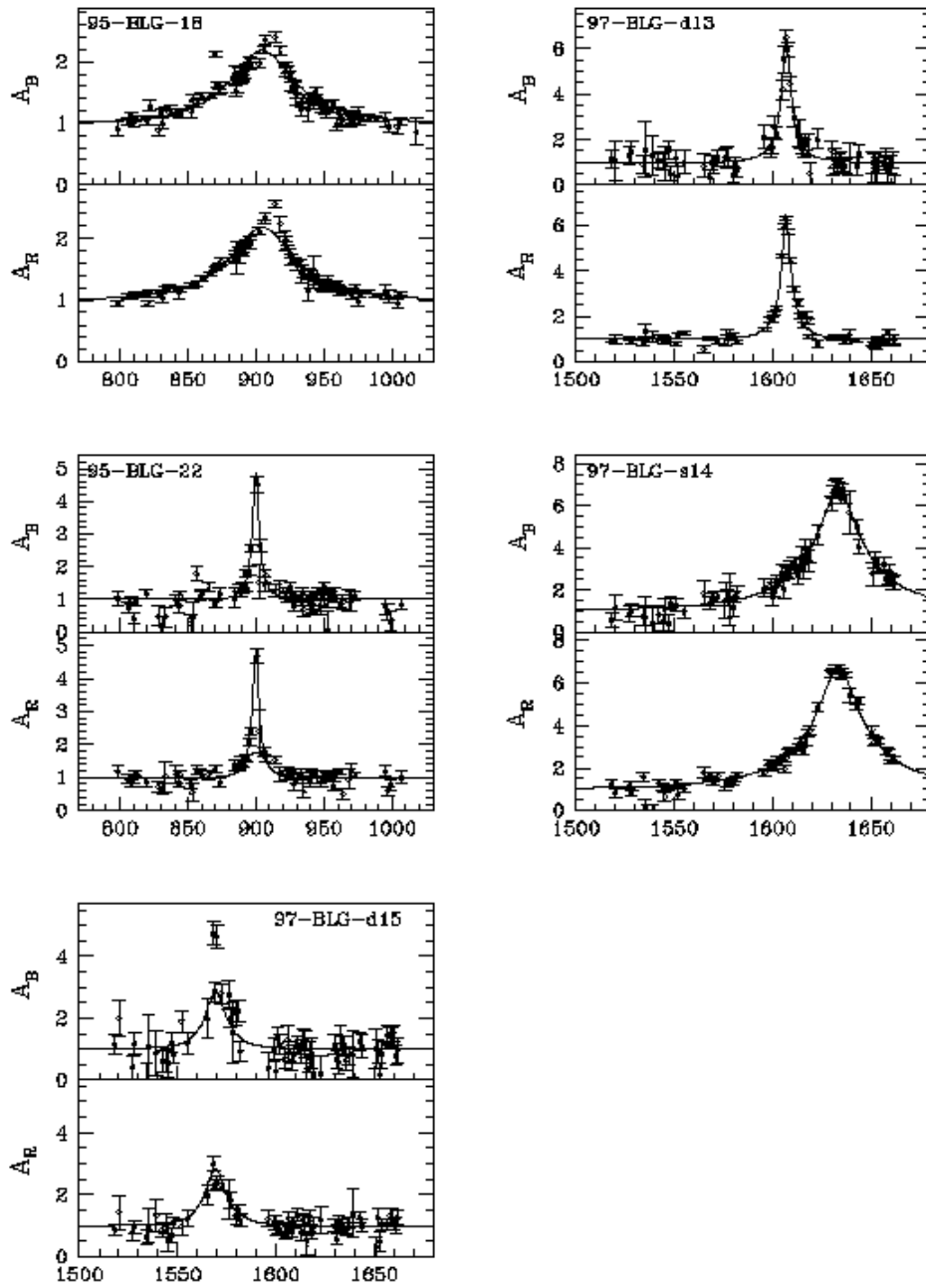


Fig. 3.— Events from Field 128. New DIA events have Ids containing “d”. New events selected with this analysis and a reanalysis of the SoDoPhot data have Ids containing “s”.



JD - 2449000

Fig. 3.— Events from Fields 128 & 159. New DIA events have Ids containing “d”. New events selected with this analysis and a reanalysis of the SoDoPhot data have Ids containing “s”.

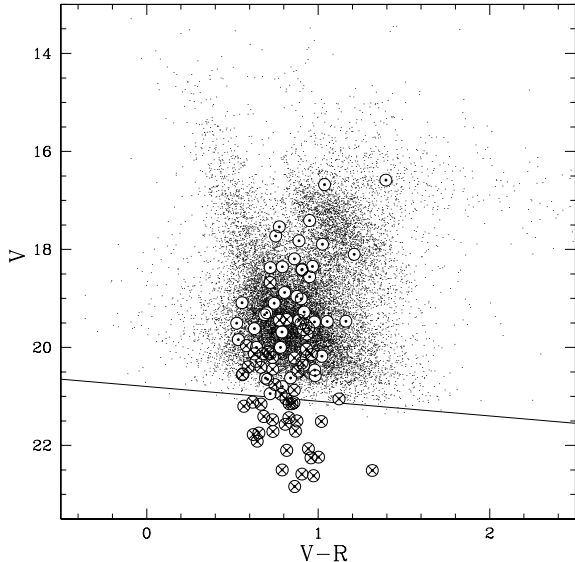


Fig. 4.— The fitted  $V$  magnitudes and colours of the microlensing events overlaid on a CMD of neighbouring resolved stars. The solid line corresponds to a pixel lensing cut. Circles with dots represent classical events and circles with crosses are pixel lensing events. Some pixel lensing event sources appear above the cut because they are not associated with monitored SoDoPhot sources.

The microlensing event’s source star  $V$ -magnitudes and  $V - R$  colours are displayed in Figure 4. This figure is an average CMD, which has been constructed by combining the SoDoPhot photometry for the  $\sim 250$  stars nearest each microlensing event source star. Notice that there are very few events with bright main sequence sources. This is to be expected, since not only are there few of these bright stars, but most of them are foreground disk stars which “see” a much lower microlensing optical depth. The SoDoPhot analysis is sensitive to microlensing events occurring with relatively bright source stars ( $V < 21$ ) or fainter stars which are blended with these monitored bright stars. The DIA technique on the other hand is sensitive to events independent of the locations of the brighter stars. In this way the DIA technique is expected to mainly detect events where the source star is faint and not blended with a bright star monitored by SoDoPhot. Events with unresolved sources are termed pixel lensing events.

### 5.1. Pixel Lensing Events

Our set of microlensing events contains both classical microlensing events and pixel lensing events. In recent years, the division between these two groups of events has been unclear because of the difference between pixel lensing and the pixel method. We will attempt to clarify this division in regard to our events. Our definition of pixel lensing derives from the theory of Gould (1996) who defined Pixel Lensing as the “gravitational microlensing of unresolved stars”. Whereas, the “Pixel Method” is a method of binning images, which is used by the AGAPE group to detect microlensing events towards M31 (Ansari et al. 1997; Gondolo 1997).

Throughout this work when we refer to pixel lensing, we shall mean: “gravitational microlensing events where the source stars are unresolved in initial template/reference images of a field”. This seems the most logical definition as it is equally applicable for events seen towards extra-galactic targets, such as M31, as it is for events in the line-of-sight to the Magellanic clouds and Galactic bulge. In contrast to this, a classical microlensing event is taken to be one where the source is resolved both before and after the lensing has taken place. As a division between classical and pixel microlensing still remains somewhat unclear, we will further refine our concept of pixel lensing.

For all the microlensing surveys presently being carried out, there is a significant amount of crowding and blending. Specifically, there are many faint unresolved stars within the seeing disk of any star bright enough to be detected. A microlensing event detected by monitoring such a *group* of stars, could be due to either a bright detectable star (classical lensing), or one of the many faint unresolvable neighbouring stars blended with it (pixel lensing).

When events are due to the unresolved faint stars, there can be a measurable shift in the flux centroid position of the event as the event brightens (Alcock et al. 1997c). However, the offset between the faint source’s centroid and the group centroid is a random quantity. Such an offset will take an arbitrarily small value in some events. Hence, this approach can not quantify the degree of blending for all events. Another property of these events is that they can exhibit a significant chromatic signature when the event’s source star colour varies from the overall colour of the group. Sources on the main sequence near our detection limit ( $V \sim 21$ ) make up the bulk of the monitored stars

and have a narrow range of colours. For this reason, in many cases, there may be little difference between an individual star’s colour and that of the blended group of stars it resides amongst. The final piece of information about blended events comes from the shape of the light curve. That is, a given amplification microlensing event has a specific shape. Once again there is only a slight difference between the shapes of events with different amplifications if various timescales are considered (see Griest & Hu 1992, Wozniak & Paczyński 1997 & Alcock et al. 1999c).

From these considerations, a sensible method of differentiating between classical and pixel microlensing events is to put limits on the allowable centroid offset, the true amount of flux (amplification), and the event’s colour. Beyond such hypothetical limits an event could be defined to be pixel lensing with significant confidence. For this reason we will set further limits on our definition of pixel lensing events. To quantify this decision we define that, for classical lensing the centroid offset between the event centroid and the nearest photometered object centroid should be less than three times the centroid uncertainty. Otherwise this is a pixel lensing event. The average uncertainty in our event centroid positions is  $\sim 0.2''$  for the results presented here. This uncertainty includes the error in the transformation between DIA and SoDoPhot templates. We thus adopt an offset of 1 pixel ( $0.63''$ ) as our classical event limit. In addition, if the microlensing event fit gives a source  $V$  magnitude which is significantly below the detection threshold (for isolated stars), the event is deemed a pixel lensing event. Because none of the stars in the observed fields are truly isolated, the actual detection threshold will be higher. Thus, this serves as a robust lower limit on classical lensing event sources. However, the uncertainty in the fitted baseline source flux increases as the brightness of the source decreases. For the analysed fields we have set this threshold limit to be  $V_{pix} < 20.8 + 0.3(V - R)$  (see Figure 4).

Measured variations between the microlensing event’s colour, and the source’s baseline colour, do not provide sufficient evidence to distinguish whether an event is due to pixel lensing or classical lensing. For some events the chromatic signature of blending can be measured in the light curve of the event, although the source is bright enough to be detected if it were isolated. Such colour changes can tell us the magnitude of the difference in the colours, and the colour of the group. But colour information does not guarantee

an event is due to an unresolvable star. However, the larger the colour differences, the more likely an event is pixel lensing.

Applying these definitions to our events we separate the classical events and pixel lensing events. Slightly different information is available for classical and pixel lensing events. With classical events there is a measured baseline flux of the source star. This baseline flux is a blend of all the stars within the seeing disk. For these events one can perform blend fits on the photometry in order to determine the true baseline source flux and hence amplification and event timescale. The fit parameters for the individual events are given in Table 5. A blended baseline flux is not applicable for pixel lensing events. However, the baseline source flux, the amplification, and the timescale can still be determined from the microlensing light curve fit, these are given in Table 6.

Two types of fits were performed for classical events: one which assumed the nearest SoDoPhot source star flux was the true source flux, and the other where the source star flux was a free parameter. The results of the first approach was expected to yield biased results because of the blended flux. However, this set is useful to examine timescale and other biases caused by blending. We fitted with the baseline source flux as a free parameter for all our pixel lensing events. This enabled us to determine the amplification of each lensing event relative to a fitted baseline flux value.

## 5.2. Comparison with the Standard Analysis

During our normal data reduction procedure we carry out a detailed reanalysis of all the SoDoPhot photometry. This reanalysis is designed to find new microlensing events and better characterise the known *alert* events. The reanalysis typically finds a few more events than the alert system as the alert scheme was designed for real time notification, and as such only includes the data reduced at the time the alert is issued.

Implementing the DIA technique we have found 41 more events than the SoDoPhot analysis using the same image data. This method thus gives us  $\sim 71\%$  more events than our approach based solely on PSF photometry. We believe this is not due to the failure of our PSF analysis, but instead is a tribute to the advantage of the new technique. To emphasise this, we point out that there are in fact 57 new events in the

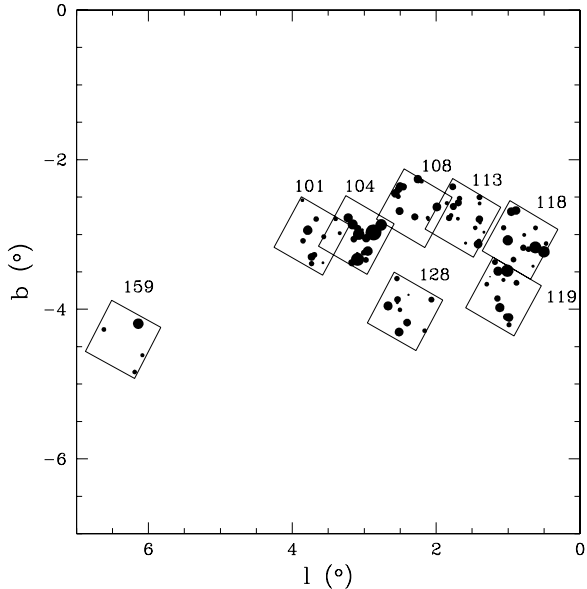


Fig. 5.— The locations of the 8 Galactic bulge fields presented in this paper are shown in Galactic coordinates (with their corresponding MACHO Id numbers). The 99 microlensing events are represented as dark spots at the event locations. The area of each spot is proportional to the  $\hat{t}$  value of the event. Baade’s Window is in field 119.

DIA which were not found in the standard SoDoPhot analysis (see Table 3). However, 16 events detected with the SoDoPhot analysis were not found with the DIA reduction. These missed events fall into a number of categories. Seven missed events were missed because of differences between the microlensing cuts used (1 low S/N event, 3 poor photometry events, 1 event with  $\hat{t} > 300$  days, 2 events fail the  $\chi_m^2$  cut). A further 4 of these events were never detected because of the slight differences between the pointing of the SoDoPhot and DIA reference images. Lastly, there is a dead amplifier on one of our CCD mosaics. Five SoDoPhot microlensing candidates fall into this location in our fields, thus photometry for these events is only available for one colour ( $B_M$ ). However, in the difference image analysis we have only analysed regions where two colour photometry is possible.

For a fair comparison of the two techniques it is necessary to compare equivalent areas of the target fields. Small differences in the pointing should not affect the overall number of events and any variation in the cuts applied is part of the reduction technique.

Therefore, to fairly compare the two sets we set aside the five single colour events in the region not analysed with DIA. We thus conclude that the SoDoPhot analysis yields 53 events compared to 99 events from the DIA technique. This method thus provides  $\sim 87\%$  more events than the standard SoDoPhot analysis.

The entire MACHO dataset consists of around 350 candidate microlensing events. A complete DIA-based reanalysis of the Galactic bulge database could therefore provide  $> 600$  events. The number of events detected towards the LMC, by SoDoPhot analysis, is still relatively small (Alcock et al. 2000a). A factor of 2 increase in the number of events detected towards the LMC would be an important way of reducing the statistical uncertainty in the microlensing optical depth and hence the baryonic fraction of the Galactic halo. We believe this factor of 2 could be achieved in a future reanalysis of LMC data with DIA.

## 6. MICROLENSING DETECTION EFFICIENCY

To determine the microlensing detection efficiency of this analysis we produced a Monte-Carlo simulation for each of the eight fields reduced. In this simulation we attempted to include all the known aspects of the analysis, such as the seeing, sky-level, transmission, systematic noise, etc., of each observation.

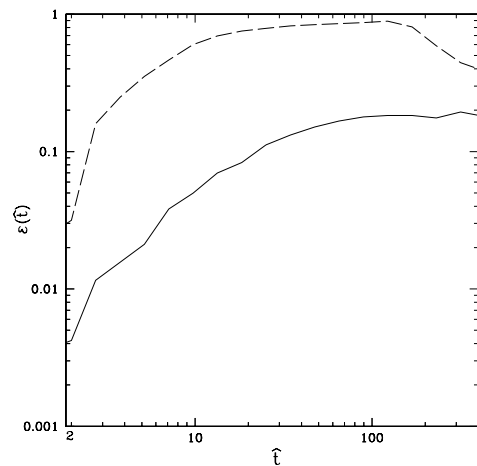


Fig. 6.— Combined microlensing detection efficiency for source stars to a limiting magnitude of  $V \sim 23$  (solid line), and for clump sources (dotted line). Efficiencies differ from these lines for individual fields because of variations in sampling, reddening seeing, etc.



The combined average detection efficiency, as a function of event timescale, is given in Figure 6. The calculation of the optical depth contribution from each microlensing event uses the efficiency for the field where the event was found.

### 6.1. The Combined Luminosity Function

The observed detection efficiency is dependent on the number and colour distribution of target source stars. In the case of pixel lensing events these stars may lie below the detection threshold of our experiment. To determine the properties of stars below our detection threshold we have used the Hubble Space Telescope (HST) Luminosity Function (LF) and colour-magnitude diagrams (CMDs) for Baade’s Window of Holtzman et al. (1998). These observations were taken with the HST Wide Fields Planetary Camera 2 (WFPC2) which has a field-of-view of  $\sim 5\text{ arcmin}$ . There are very few bright stars ( $V < 16$ ) in these HST data, so the bright end of the luminosity function is not well defined from these data alone. However, the MACHO camera’s field-of-view is hundreds of times larger than that of WFPC2 ( $43' \times 43'$ ), so many bright stars are in the MACHO observations of Baade’s Window. We thus combine the luminosity function and CMD of Holtzman et al. (1998) with those of our field 119 (our Baade’s Window field).

To combine these data we transformed the Holtzman et al. (1998)’s HST photometry from ( $F555 - F814$ ) to Landolt’s ( $V - I$ ) with the calibration given in Holtzman et al. (1995). The HST magnitudes were converted to *Kron-Cousins*  $V - R$  with the transformations of Bessell (1995). For MACHO data we used the conversion from  $R_M$  and  $B_M$  to *Kron-Cousins*  $V$  and  $R$  given in Alcock et al. (1999c). We note this calibration varies slightly from the most recent determination given in Alcock et al. (1999a). The two data sets were combined at  $V \sim 18.5$  where the MACHO detection efficiency starts to decrease from unity. The uncertainty in the number of stars from the combined LF is 9.5%. This uncertainty carries through to our optical depth estimate with the same magnitude. The number of stars in each of our 8 fields is calculated using this combined luminosity function and the measured stellar density of clump stars relative to field 119. By taking this approach we have implicitly assumed that the stellar density does not vary greatly within Baade’s Window.

A major cause of variations in the apparent stellar density towards the Galactic center is the patchy

extinction caused by dark dust clouds. However, Baade’s Window is well known as a region of low extinction. Furthermore, the extinction in Baade’s Window appears to be relatively homogeneous (Alcock et al. 1997d). Therefore, we believe that the combined LF should only be slightly affected by extinction inhomogeneities. We have also made the assumption that the morphology of the CMD does not vary between the HST field and the MACHO one. We expect that the presence of the Galactic bar (Paczynski et al. 1994) could cause the number of clump giants to vary slightly across our Baade’s Window field.

### 6.2. Artificial Events

To simulate microlensing events, firstly we weighted the  $V$ -magnitude axis of the combined (HST+MACHO) CMD to reflect the luminosity function distribution. We then binned this CMD and determine the relative probability of selecting a source star in any given bin. Next, we randomly selected a source star for the event based on the bin probability. A random impact parameter  $u_{min}$ , timescale  $\hat{t}$ , and time at maximum  $t_{max}$  were then assigned to the artificial event. An artificial image was produced for each observation and the artificial source star was added. Each image is only  $\sim 25'' \times 25''$  in size. These images were further populated with neighbouring so called *blend-stars*. These stars were selected from the CMD in the same way as the source star and allow us to simulate the effect of blending on light curves. The number of blend-stars we added to the images was based on the observed stellar density of the field we were simulating. Each of the artificial stars was placed at a random location within the artificial image. An artificial image was made for each observation of the event. These images were produced with seeing conditions that matched those observed during the data reduction.

For each simulated lensing event we performed photometry on the set of artificial images making up the light curve. This photometry included the uncertainties produced by the photon and systematic noise of all the stars contributing to the flux aperture. The photometry of each of the simulated events was piped through the detection and selection processes used in the real analysis to determine the overall efficiency.

The simulation was performed separately on each of the eight Galactic bulge fields using the seeing conditions, sky background level, etc., of the field selected. For each field we produced 100,000 artificial microlensing events each with  $\sim 300$  observa-

tions. The seven fields adjacent to Baade’s Window were simulated using the combined Baade’s Window luminosity function. In each case the LF and the combined CMD were reddened to the average reddening of each field. Since the fields are at Galactic latitudes spanning  $\sim 2^\circ$  we expect the contributions from the number of disk stars and bulge stars to vary between fields. The stellar densities in simulation of each field were adjusted to reflect the observed densities. These field-dependent stellar densities were employed because the amount of blending is dependent on the observed density.

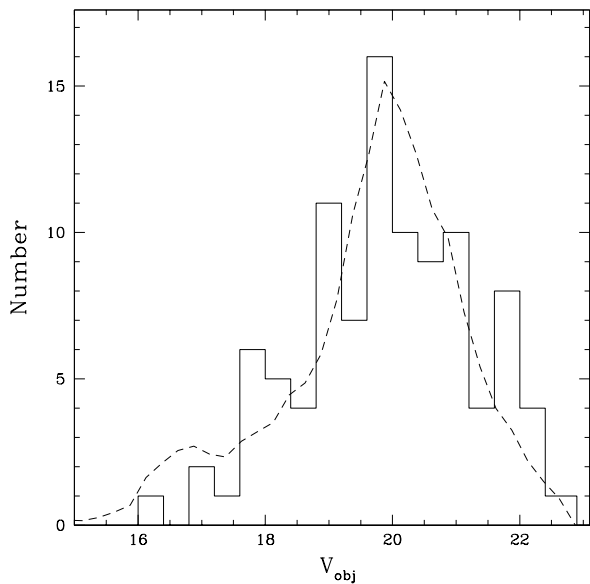


Fig. 7.— The distribution of source magnitudes. The solid histogram shows the distribution of the events in  $V_{obj}$  corrected to the average reddening of field 119 (Baade’s Window). The dashed line is the luminosity function modified by the efficiency and normalised to the area of the histogram.

To compare the results from our simulation with the observed distribution of events, we have plotted the actual (histogram) and expected (dashed line)  $V$ -magnitude distributions in Figure 7. In this plot we have multiplied the Baade’s Window LF by the detection efficiency, thus giving the expected source star  $V$ -magnitude distribution. The microlensing event source star magnitudes ( $V_{obj}$ ) have been extinction corrected to the average reddening observed in our Baade’s Window field. The good agreement between

these two distributions suggests that our simulated efficiency analysis reproduces the actual detection sensitivity quite well. For further details of the detection efficiency simulation, see Drake (2000).

## 7. THE OPTICAL DEPTH

The microlensing optical depth is defined as the probability that any given star is microlensed with impact parameter  $u_{min} < 1$  (i.e.  $A_{max} > 1.34$ ) at any given time. This optical depth is independent of the mass of the lensing objects, so no assumption is required about velocity distributions and mass functions. The optical depth can be estimated by,

$$\tau_{est} = \frac{\pi}{4N_*T_*} \sum_i \frac{\hat{t}_i}{\epsilon(\hat{t}_i)}. \quad (5)$$

$N_*$  is the number of stars and  $T_*$  is the exposure time of the experiment in years,  $\hat{t}_i$  is the Einstein ring crossing time for the  $i$ th event, and  $\epsilon(\hat{t}_i)$  is the detection efficiency for a given event timescale. In this analysis we use the source fit  $\hat{t}$  values, given in Tables 5 and 6, to determine the optical depth. For the *exotic*: finite source, binary lensing and parallax affected events, we use the  $\hat{t}$  values given in Alcock et al. (1997a, 2000b & 2000c). For microlensing events with timescales which our experiment is sensitive to (2 – 300 days), we obtain  $\tau_2^{300} = 2.43_{-0.29}^{+0.31} \times 10^{-6}$ . When we include the uncertainty in the effective number of stars monitored, we obtain  $\tau_2^{300} = 2.43_{-0.38}^{+0.39} \times 10^{-6}$ .

The statistical uncertainties in the optical depth have been obtained by using the fact that the number of events obey Poisson statistics. We have simulated “experiments”, where the number of observed events  $N$ , follows a Poisson distribution. For each event in the simulated timescale distribution we randomly assign one of our measured event timescales (see also Udalski et al. 1994; Alcock et al. 1997b). The optical depth for each of these distributions is then evaluated. Counting the fraction of these experiments which yield a larger optical depth than our measured value  $\tau$ , allows us to determine the statistical distribution of optical depth. This distribution is shown in Figure 8, from which we determine confidence limits on our measured optical depth  $\tau_{meas}$ .

The simple geometry of microlensing events results in the theoretical prediction of a linear distribution in impact parameters ( $u_{min}$ ). However, experimentally events with faint source stars require larger magnifications to be detected. This tendency skews the impact

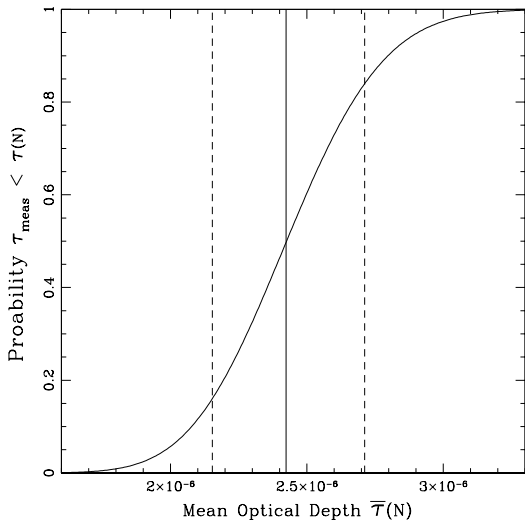


Fig. 8.— The distribution of statistical uncertainty in the microlensing optical depth from Monte-Carlo simulation for our 99 event sample. The dashed lines mark one  $\sigma$  confidence limits. The solid line gives the observed optical depth.

parameter distribution towards smaller  $u_{min}$  values. The effect of this is clearly seen in the cumulative distribution shown in Figure 9.

A Kolmogorov-Smirnov (K-S) test is a useful method for comparing whether samples of events are drawn from the same distribution. A comparison between the expected distribution from our efficiency analysis and that observed, gives a K-S statistic of  $D = 0.086$ . This corresponds to a probability of  $P(KS) = 0.39$ . In a comparison between the observed distribution and a uniform distribution, we get a K-S statistic of  $D = 0.338$  corresponding to  $P(KS) = 5.78e^{-10}$ . The observed  $u_{min}$  distribution is only compatible with that found using our efficiency simulation, which demonstrates the bias towards high amplification events.

### 7.1. The Optical Depth in Individual Fields

The microlensing optical depth is a measure of the mass in lensing objects along a line-of-sight. This quantity is independent of the individual masses of lensing objects, as long as they have characteristic timescales which lie within the region to which the experiment is sensitive. To calculate this statistic from the measurements we do not need to know the velocity

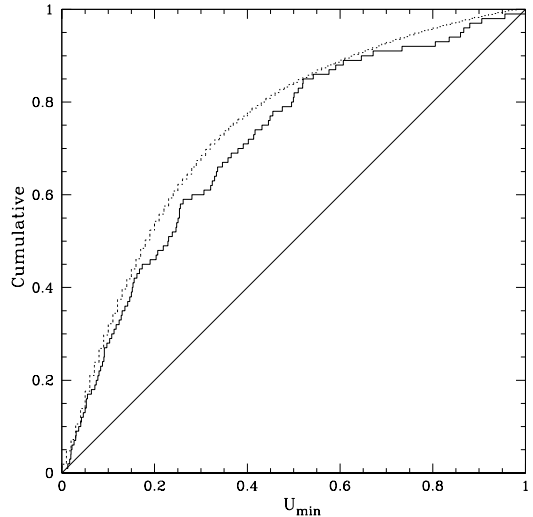


Fig. 9.— The cumulative distribution of impact parameter for the 99 microlensing event sample. Here the straight line shows the expected  $u_{min}$  distribution for microlensing without the effect of efficiency. The dotted histogram show the distribution for the efficiency simulation and the solid histogram the observed distribution.

or mass distributions of the object causing the lensing. This value is therefore useful to compare the measurements with the predictions from Galactic models, where the distribution are assumed. However, any Galactic models which match the observed total optical depth must also match the observed event timescale distribution. Event timescales provide a constraint on a model’s velocity and mass function. By splitting the dataset of observed events into subregions, one can also compare the optical depth distribution as a function of location.

Since we expect the relative number of disk stars and bulge stars to vary between fields we decided to model this variation. To account for this we produced a disk-LF by combining the LFs of Wielen, Jahreiss, & Krüger (1983) and Gould, Bahcall, & Flynn (1996) at  $M_V = 9$ . The result is a luminosity function for the disk ranging from  $M_V = -1$  to  $M_V \sim 14$ . We assume that the disk is well modeled by the standard double exponential disk density profile given by,

$$\rho_d = \rho_{d0} \exp\left(\frac{-|z'|}{h} + \frac{(R_0 - s)}{s_d}\right). \quad (6)$$

For, the disk cylindrical galactocentric coordinates  $(s, z')$ , we have  $s^2 = 1 + z^2 \cos^2 \theta - 2z \cos b \cos l$ , and  $z' = z \sin b$ , where  $z = D_d/D_{8.5}$  and  $s_d$  is the disk scale length (2.5 – 3.5 kpc). The mass density in the solar neighbourhood is given by  $\rho_{d0}$  ( $0.05 M_{\odot} \text{pc}^{-3}$ ), and  $h$  is the scale height of the disk.

We use this double exponential disk model to determine the form of the disk-LF that we expect in each of our fields, with proper consideration of the reddening and the number of stars within the observed volume. Here we assumed a disk scale height  $h$  of 325 pc and a scale length  $s_d$  of 3 kpc. We normalised the disk-model luminosity function for each field to the number of disk stars, observed in the magnitude range  $14 < V < 18$ . This allowed us to approximate how many disk stars there are in each field down to the source star magnitude limit ( $V = 23$ ). The percentage of disk stars at this limit,  $p$ , was given in Table 3. By subtracting the disk-model LF for the Baade’s Window field from the HST+MACHO combined LF, we were able to determine the bulge luminosity function. We then assumed that the number of bulge stars in our fields were traced by the number of clump giant stars. The detection completeness for these bright clump stars is nearly 100%, so these stars serve as a good tracer of the number of fainter bulge main sequence stars, where our detection completeness is low and uncertain. We scaled our disk-subtracted bulge luminosity function by the ratio of the number of clump stars in each field relative to our Baade’s Window field,  $r$  (Table 3). We finally determined the total number of stars in each field by combining the number of disk stars from our disk model, and bulge stars from the scaled Baade’s Window bulge luminosity function.

The optical depth for each individual field (given in Table 3) was determined using the total number of stars in each field. From the tabulated data it seems there is a trend in optical depth with Galactic latitude and a weaker trend with longitude, as is expected. However, the observed optical depth for field 104 appears to break from the general trend, although the uncertainties for this field are quite large. The density of stars in field 104 is not significantly higher than the other fields ( $N_{104} \approx N_{108}$ ), and this evidence naturally leads us to believe that the number of faint lensing stars should be similar. A group or cluster of low-mass, faint stars in the foreground of the field could go undetected in our photometry and would act as efficient lenses. There is a globular clus-

ter in field 104 and another nearby, but the locations of these do not appear to coincide with the observed microlensing events.

## 7.2. Uncertainties in the Optical Depth

The major cause of uncertainty with the determined optical depth could be erroneous values from the microlensing fits. For low S/N events it is difficult to determine whether the correct amplifications and  $\hat{t}$  values have been found. For such events there are similarities between the light curves of events with different timescales and amplifications (Wozniak & Paczyński 1997). However, Han (2000) has recently shown that fits to high amplification pixel lensing events do give accurate results.

In this analysis we have used a single CMD to determine the microlensing detection efficiency of the analysis. This CMD is artificially reddened to the average value determined for each field, which assumes that the morphology of the CMD does not vary much between these fields. From our disk model it appears that the number of disk stars relative to bulge stars varies little from field to field. The gradient in the observed optical depth is in part due to the dependence of the numbers of disk stars on the Galactic latitude. If our assumed model of the disk is in error, the number of stars we determine for the individual field will be incorrect. This will also affect our disk-subtracted bulge luminosity function. However, the calculated number of disk stars is only about 10% of the total number of stars in any field, in good agreement with Zoccali et al. (2000), so this effect should be small. Our total optical depth result is less dependent on the assumed disk model than the individual fields, since the ratio of the total number of disk stars ( $14 < V < 18$ ) to clump stars in all 8 fields combined, is very close to the ratio of disk to clump stars in Baade’s Window.

In addition, the extinction in each observed field is taken into account using values determined from the RR Lyrae stars in each field (Alcock et al. 1998). There are small uncertainties in the efficiencies due to variations in reddening within a field. This should not affect the overall optical depth but may be important for estimates in individual fields.

## 8. THE STRUCTURE OF THE GALAXY

We will now review what has been reported about each of the Galactic features that have the largest

effect on the observed microlensing optical depth. For each of these we will discuss whether our results are consistent with models and previous determinations.

### 8.1. Bar Orientation

The optical depth is highly dependent on the position angle of the bar (Peale 1998) and bulge mass (Gyuk 1999). The observational results for the bulge inclination based on a number of different types of observations give conflicting values ranging from  $16^\circ$  to  $44^\circ$ , see Table 7. A bar inclined at the large angle reported by Sevenster et al. (1999) is not an efficient source of lensing events. The size of our observed optical depth favours the smallest possible bar inclination angle. However, the bar is insufficient to produce an optical depth greater than  $\sim 2.5 \times 10^{-6}$  even for models with a small bar inclination angle, and a large bar mass (see Peale 1998).

### 8.2. Bar Mass

Ideas to explain the observed microlensing optical depth with values of bulge mass are also not clear-cut. Based on COBE map data Zhao & Mao (1996) found  $M_{bulge} = (2.2 \pm 0.2) \times 10^{10} M_\odot$ , yet Dwek et al. (1995) found a mass of only  $1.3 \times 10^{10} M_\odot$ . Bissantz et al. (1997) found that, based on DIRBE results, within 2.4 kpc of the Galactic center the combined bulge plus disk mass is  $1.9 \times 10^{10} M_\odot$ . However, only  $0.72 - 0.86 \times 10^{10} M_\odot$  of this is attributed to the bulge mass. This is consistent with Holtzman et al. (1998)'s results ( $0.74 - 1.5 \times 10^{10} M_\odot$ ).

Predictions of the Galactic bar mass have also been discrepant. Based on the virial theorem, Han & Gould (1995) predicted that  $M_{bar} = 1.6 \times 10^{10} M_\odot$ , as did Kent (1992) based on a simple oblate rotator model. But Blum (1995) predicted  $M_{bar} = 2.8 \times 10^{10} M_\odot$  when pattern rotation of the Galactic bar is included. Zhao & Mao (1996) determined that a bar mass of at least  $> 2.0 \times 10^{10} M_\odot$  is required for the COBE G1 model (with  $\theta = 11$  degrees) to account for observed amount of lensing. The Zhao & Mao 1996 model is consistent with Alcock et al. (1997a)'s microlensing data at the  $2 \sigma$  level, if a bar mass of  $2.8 \times 10^{10} M_\odot$  is used. Gyuk (1999) advocated  $M_{bulge} = 2.5 \times 10^{10} M_\odot$  based on a maximum likelihood estimate of the COBE G2 model, where a small inclination angle of  $\theta = 12$  degrees was assumed. However, if  $\theta$  was instead taken to be 20 degrees (consistent with most of the values in Table 7), the most

likely bulge mass rises to  $\sim 3.6 \times 10^{10} M_\odot$ . A heavy bar is favoured for our observed optical depth, but as yet there is no evidence that the bar is massive enough to produce the observed optical depth. It is clear that more accurate measurements are necessary to better constrain the bar mass used in models. In Table 8 we present the optical depths for a number of Galactic models for comparison with our result.

### 8.3. The Disk

The estimates of the optical depth due to the disk also exhibit a range of values. Spiral arms may contribute  $0.5 \times 10^{-6}$  (Fux 1997). A truncated disk would contribute  $0.37 - 0.47 \times 10^{-6}$  (Paczynski 1991), whereas a full disk would contribute  $0.63 - 0.87 \times 10^{-6}$  (Zhao, Spergel, & Rich 1995). However, from these values it is clear that the disk is expected to be a less important contributor to the optical depth than bar mass or bar orientation. The only measurement of the contribution of disk lensing comes from the EROS II analysis ( $0.38_{-0.15}^{+0.58} \times 10^{-6}$ , Derue et al. 1999). This is in good agreement with predictions, but is based on just three microlensing events.

We have estimated a disk lensing contribution to the optical depth of  $f_{disk} \sim 25\%$ . This gives  $\tau_{bulge} = 3.23_{-0.50}^{+0.52} \times 10^{-6} [0.75 / (1 - f_{disk})]$ . Disk lenses are not expected to contribute much more than 25% since there is little evidence of any disk-disk lensing of the foreground main sequence stars in Figure 4. However, the optical depths we observed in the individual Galactic bulge fields are quite high and are thus consistent with a large disk optical depth.

### 8.4. The Timescale Distribution

The mass function of the compact objects in the Galaxy has a direct effect on the timescales of microlensing events. To date, few authors have attempted to reproduce simultaneously both the optical depth and the timescale event distribution. The agreement between models and observations under these two constraints is necessary, if any confidence is to be put in the models. Peale (1998) and Méra et al. (1998) have found that the Galactic models poorly reproduce the observed timescale distribution of Alcock et al. (1997a).

#### 8.4.1. Short Timescale Events

The geometry of microlensing produces short timescale events where the lenses are either near the observer

or the source. However, variation in the lens location has only a small effect, unless either the observer-lens distance or lens-source distance is very small. Short timescale events can also be produced by low mass lenses, but the timescale goes as  $M^{1/2}$ , so the effect is small. Distributions with a significant number of short timescale events and a number of long timescale events, point to a large range of lens masses.

In an attempt to reproduce the observed short timescale events of Alcock et al. (1997b), mass functions with large numbers of low mass objects, such as brown dwarfs, have been produced (Méra et al. 1998; Peale 1998; Han & Chang 1998). This is supported by recent discoveries of free floating brown dwarfs (Reid et al. 1999; Cuby et al. 1999). But there is still controversy surrounding whether this will (Han & Chang 1998), or will not (Peale 1999) reproduce the expected timescales correctly. If the short timescale events are not brown dwarf lensing events, then this indicates a large population of low mass stars in the bulge. It is possible that a large number of M-type stars might better explain the timescale distribution (Peale 1998), but this does not appear to be consistent with the shallow slope of the mass function found in recent deep observations of the Galactic bulge (Holtzman et al. 1998; Zoccali et al. 2000).

#### 8.4.2. Long Timescale Events

The timescale distributions from contemporary Galactic models also do not reproduce the observed number of long timescale events,  $\hat{t} > 140$  days (for example, see Alcock et al. 1997b; Han & Gould 1996; Méra et al. 1998; Peale 1998). With the data of Alcock et al. (1997b) it was unclear whether these long timescale events were a real population or a statistical anomaly. For long timescale events we expect either large lens masses, low transverse velocities, or equal observer-lens and lens-source distances. Disk-disk lensing events are expected to give long timescale events because of the low velocity dispersion of the disk. Long timescale events have been observed for known disk-disk lensing events (Derue et al. 1999). However, disk-disk lensing events are considered in the Galactic models and are constrained by star counts. The variation in lens-observer and observer-source distances has a relatively small effect on an events timescale (factor of  $\sim 2$ ). If the lenses are normal main sequence stars, their luminosities can easily be related to their masses. Owing to this relation, for nearby lenses we can impose an upper-limit

to the lens mass, given an upper-limit to the lens' luminosity (from the microlensing fits). This constrains the proximity of bright lenses to the observer (Alcock et al. 1997a). However, reddening towards the Galactic bulge is patchy and weakens this argument. One possibility is that there exists some unknown population of dynamically cold or massive, dark objects in the Galactic disk.

#### 8.4.3. The Observed Timescale Distribution

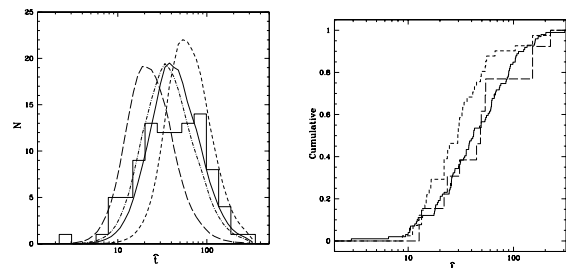


Fig. 10.— Left: the timescale ( $\hat{t}$ ) of the 99 candidate microlensing events compared to predictions from four mass models, normalised to the observed number of events. The mass functions are: a  $\delta$  function at  $0.1M_{\odot}$  (long-dashed line); a  $\delta$  function at  $1M_{\odot}$  (the short-dashed line); a Scalo (1986) PDMF (solid line); the Han & Gould (1996) power-law model with  $\alpha = -2.3$  and  $m_{lo} = 0.1$  (dash-dotted line). Right: the cumulative timescale distributions of the events from this work (solid line). The Alcock et al. (1997e) full sample of 41 events (short-dashed line) and the Alcock et al. (1997e) 13 clump giants (long-dashed line). The results are consistent with the 13 clump sample but not with the 41 event sample which are affected by blending problems.

The microlensing event timescale distribution is plotted in Figure 10. Here we have over-plotted the timescale distribution expected for four mass functions assuming the barred bulge, given in equations (3) and (4), plus a double exponential disk density model given in (Alcock et al. 1997b). These four mass models are: a Scalo (1986) main sequence present day mass function (hereafter PDMF), two  $\delta$  function distributions ( $0.1M_{\odot}$  &  $1M_{\odot}$ ), and the power-law distribution of Han & Gould (1996) ( $\alpha = -2.3$ ,  $0.1 < m < 1.4M_{\odot}$ ). The agreement between the Scalo (1986) mass model and event timescale distributions appears quite reasonable. This might imply that the microlensing events seen towards the Galactic bulge

can be explained by the observed distribution of stars, if they follow a Scalo (1986) mass model. However, this does not explain the large observed optical depth. The timescale distribution also appears to be somewhat broader and much less peaked than expected. This difference could possibly be due to uncertainties in the timescales of the fainter events. There does not appear to be a large population of short timescale events in the distribution. This implies there is probably not a large population of brown dwarfs along the bulge line-of-sight. However, there is some evidence for a population of long timescale microlensing events, as there are seven events with timescales  $\hat{t} > 140$  days.

In the right panel of Figure 10 we present the cumulative distribution of event timescale for these results compared with our previous results for the Galactic bulge. Here we find relatively few short timescale events compared to the previous results of Alcock et al. (1997b), where fits did not include parameters for the blended flux component. A K-S statistic comparison between the cumulative distributions of the events from Alcock et al. (1997b) and this analysis gives a K-S statistic  $D = 0.296$ , corresponding to a probability  $P(KS) = 0.0154$ . This indicates that there is a significant difference between the two timescale distributions. The fact that blending will bias the event timescale distribution to shorter values has been known for many years (Nemiroff 1994) and has been studied in detail by a number of authors (Alcock et al. 1996; Wozniak & Paczyński 1997; Alard 1997; Han 1997; Han et al. 1998). Therefore, this result is not surprising. We note that a small fraction of the difference between these and the previous results is also due to difference between the detection efficiencies of Alcock et al. (1997b) and those of this analysis. In a comparison with the 13 clump giant sample of Alcock et al. (1997b) we get a K-S statistic of  $D = 0.25$  corresponding to  $P(KS) = 0.37$ . Our results are thus consistent with the clump giant microlensing events. Clump giant microlensing events are less affected by blending since they generally are much brighter than the stars with which stars they are blended. This suggests that, as expected, our microlensing timescale distribution is less biased by blending than the distribution of 41 events given in Alcock et al. (1997b).

The efficiency corrected timescale distributions are presented in Figure 11. From the right panel of Figure 11 one can also see that the optical depth for this sample of events is not dominated by the long

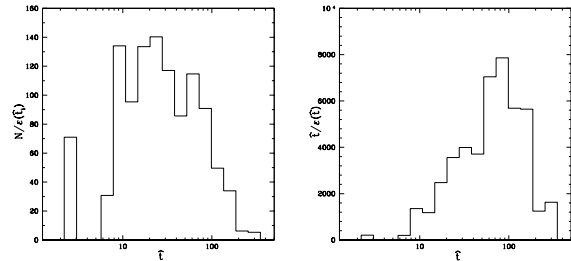


Fig. 11.— Left: a histogram of the  $\hat{t}$  distribution corrected to 100% efficiency (The expected true event timescale distribution.). The first bin in the distribution is a lower estimate as the efficiency has been truncated at 2 days where events are too short to be detected in this analysis. Right: the contribution to the overall microlensing optical depth ( $\tau$ ) of the observed event timescale distribution.

timescale events as it was in Alcock et al. (1997b). The present optical depth determination is less dependent on a small number of long timescale events. However, the relative contribution of each individual long timescale event is still large compared to short ones because of the detection efficiency.

## 9. SUMMARY

We have presented the results from the DIA survey of MACHO Galactic bulge data. In this analysis we detect 99 microlensing events in eight fields. This survey covers three years of data for  $\sim 17$  million stars to a limiting magnitude of  $V \sim 23$ . Our result is consistent with the detection of 75–85% more events than an analysis performed with PSF photometry on the same data.

We have measured a microlensing optical depth of  $\tau = 2.43^{+0.39}_{-0.38} \times 10^{-6}$  for events with timescales between 2 and 300 days. With consideration of the disk-disk component we find a Galactic bulge microlensing optical depth of  $\tau_{bulge} = 3.23^{+0.52}_{-0.50} \times 10^{-6} [0.75 / (1 - f_{disk})]$ . These optical depth determinations are consistent with the previous 45 event analysis and 13 event clump giant sub-sample of Alcock et al. (1997b), and the value determined by the OGLE group (Udalski et al. 1994).

For the individual fields we find that there is a trend in optical depth with longitude and latitude as expected, although there is some evidence of fine structure within the optical depth spatial distribu-

tion. However, it is difficult to set limits on this as the uncertainties for each field are quite large.

We find that our timescale distribution is compatible with lenses having masses distributed in the same way as the PDMF of Scalo (1986). We note that the timescale distribution of Alcock et al. (1997b) was biased towards shorter events by blending, making it appear that many low mass objects were required to explain the observed distribution. With our new unbiased sample, we do not require a large population of brown dwarfs towards the Galactic centre to reproduce the measured timescale distribution. It is still unclear whether or not there is an anomalous population of long timescale events.

The measured microlensing optical depth is a lower limit to the true value as events shorter than few days or longer than a few hundred would not be detected in this analysis. Nevertheless, the values presented here still appear to be larger than those predicted by most Galactic models with a bar mass and inclination consistent with observations. Such models might be better constrained by attempting to reproduce the optical depth, the observed timescale distribution and the observed optical depth gradient measured here.

We are grateful to S. Chan, M. MacDonald, S. Sabine and the technical staff at the Research School of Astronomy and Astrophysics<sup>19</sup> for their skilled support of the project. This work was in part performed under the auspices of the U.S. Department of Energy by University of California Lawrence Livermore National Laboratory under contract No. W-7405-Eng-48. Work at the Center for Particle Astrophysics at the University of California, Berkeley is supported by NSF grants AST 88-09616 and AST 91-20005. Work at Mount Stromlo and Siding Spring Observatories is supported by the Australian Department of Industry, Technology and Regional Development. K. G. and T. V. acknowledge support from DoE under grant DEF0390-ER 40546. W. J. S. is supported by a PPARC Advanced Fellowship. C. W. S. is grateful for support from the Sloan, Packard and Seaver Foundations. D. M. is supported by Fondecyt 1990440. This work was carried out by A. J. D. in partial fulfillment of the requirements for the degree of PhD at ANU.

## REFERENCES

Alard, C. 1997, *A&A*, 321, 424

<sup>19</sup>Formerly Mount Stromlo Observatory.

- Alard, C. 1999, *A&A*, 343, 10
- Alard, C., & Lupton, R. H. 1998, *ApJ*, 503, 325
- Alcock, C., et al. 1995, *ApJ*, 454, L125
- Alcock, C., et al. 1996, *ApJ*, 461, 84
- Alcock, C., et al. 1997a, *ApJ*, 491, 436
- Alcock, C., et al. 1997b, *ApJ*, 479, 119
- Alcock, C., et al. 1997c, *ApJ*, 486, 697
- Alcock, C., et al. 1997d, *ApJ*, 474, 217
- Alcock, C., et al. 1998, *ApJ*, 492, 190
- Alcock, C., et al. 1999a, *PASP*, 111, 1539
- Alcock, C., et al. 1999b, *ApJ*, 521, 602
- Alcock, C., et al. 1999c, *ApJS*, 124, 171
- Alcock, C., et al. 1999d, *ApJ*, 518, 44
- Alcock, C., et al. 2000a, preprint (astro-ph/0001272)
- Alcock, C., et al. 2000b, preprint (astro-ph/9907369)
- Alcock, C., et al. 2000c, in preparation
- Ansari, R., et al. 1997, *A&A*, 324, 843
- Aubourg, E., & Palanque-Delabrouille, N. 1999, *New Astronomy*, 4, 265
- Bennett, D. P., et al. 1993, *AAMS*, 183, 7206
- Bertelli, G., et al. 1995, *AA*, 301, 381
- Bessell, M. 1995, *PASP*, 107, 672
- Binney, J., et al. 1991, *MNRAS*, 252, 210
- Binney, J., Gerhard, O. E., & Spergel, D. S. 1997, *MNRAS*, 288, 365
- Bissantz, N., et al. 1997, *MNRAS*, 289, 651
- Blum, R. D. 1995, *ApJ*, 444, L89
- Crotts, A. P. S. 1992, *ApJ*, 399, L43
- Cuby, J. G., et al. 1999, *AJ*, 349, L41
- de Vaucouleurs, G. 1964, in *IAU Symposium 20: The Galaxy and the Magellanic Clouds*, ed. F. J. Kerr & A. W. Rogers (Canberra: Australian Academy of Science, MSSSO), 195



- Derue, F., et al. 1999, *A&A*, 351, 87
- Drake, A. J. 2000, PhD thesis, Australian National University, Australia
- Dwek, E., et al. 1995, *ApJ*, 445, 716
- Evans, N. W. 1994, *ApJ*, 437, L31
- Evans, N. W., et al. 1998, *ApJ*, 501, L45
- Fux, R. 1997, *A&A*, 327, 983
- Gondolo, P. 1997, in *Dark and Visible Matter in Galaxies*, ASP Conference Series V 117, ed. P. Massimo & S. Paolo (Sesto Pusteria: Astronomical Society of the Pacific), 281
- Gould, A. 1996, *ApJ*, 470, 201
- Gould, A., Bahcall, J. N., & Flynn, C. 1996, *ApJ*, 465, 759
- Grenacher, L., et al. 1999, *A&A*, 351, 775
- Griest, K., et al. 1991, *ApJ*, 372, L79
- Griest, K., & Hu, W. 1992, *ApJ*, 397, 362
- Gyuk, G. 1999, *ApJ*, 510, 205
- Hafner, R. M., et al. 1999, preprint (astro-ph/9905086)
- Han, C., & Gould, A. 1995, *ApJ*, 449, 521
- Han, C., & Gould, A. 1996, *ApJ*, 467, 540
- Han, C. 1997, *ApJ*, 484, 555
- Han, C., & Chang, K. 1998, *MNRAS*, 299, 1040
- Han, C., Jeong, Y., & Kim, H. 1998, *ApJ*, 507, 102
- Han, C. 2000, *MNRAS*, 312, 807
- Holtzman, J. A., et al. 1995, *PASP*, 107, 1065
- Holtzman, J. A., et al. 1998, *ApJ*, 115, 1946
- Kent, S. M. 1992, *ApJ*, 387, 181
- Méra, D., Chabrier, G., & Schaeffer, R. 1998, *A&A*, 330, 937
- Nemiroff, R. J. 1994, *ApJ*, 435, 682
- Nikolaev, S., & Weinberg, M. D. 1997, *ApJ*, 487, 885
- Paczynski, B. 1991, *ApJ*, 371, L63
- Paczynski, B., et al. 1994, *ApJ*, 435, L113
- Peale, S. J. 1998, *ApJ*, 509, 177
- Peale, S. J. 1999, *ApJL*, 524, L67
- Phillips, A. C., & Davis, L. E. 1995, in *Astronomical Data Analysis Software and Systems IV*, ASP Conference Series V 77, ed. R. A. Shaw, H. E. Payne, & J. E. Hayes (Astronomical Society of the Pacific), 297
- Reid, I. N., et al. 1999, *ApJ*, 521, 613
- Scalo, J. M. 1986, *Fund. Cosmic Phys.*, 11, 1
- Sevenster, M. J., et al. 1999, *MNRAS*, 307, 584
- Stanek, K. Z., et al. 1997, *ApJ*, 477, 163
- Tomaney, A. B., & Crofts, A. P. S. 1996, *AJ*, 112, 2872
- Udalski, A., et al. 1994, *Acta Astronomica*, 44, 165
- Vallee, J. P. 1995, *ApJ*, 454, 119
- Weiner, B. J. 1996, in *IAU Symposium 169: Properties of the Galactic Bar from Hydrodynamical Simulations*, ed. L. Blitz & P. Teuben (The Hague: Kluwer), 145
- Weiner, B. J., & Sellwood, J. A. 1999, *ApJ*, 524, 112
- Wielen, R., Jahreiss, H., & Krüger, R. 1983, in *Nearby Stars and the Stellar Luminosity Function*, ed. A. G. Philip & A. R. Upgren (IAU Coll. 76), 163
- Wozniak, P., & Paczynski, B. 1997, *ApJ*, 487, 55
- Zhao, H., Spergel, D. N., & Rich, R. M. 1995, *ApJ*, 440, L13
- Zhao, H., & Mao, S. 1996, *MNRAS*, 283, 1197
- Zoccali, M., et al. 2000, *ApJ*, 530, 418

TABLE 1  
PARAMETERS OF LEVEL-1.0 CUTS.

Cut type		Cut level	
generic var.	66.6% pts, $F_i < (F_{\text{med}} + 4\sigma_i)^{\text{a}}$	54.5% pts, $F_i < (F_{\text{med}} + 2.5\sigma_i)^{\text{a}}$	31% pts, $F_i < (F_{\text{med}} + 1.5\sigma_i)^{\text{a}}$
transient var.	90% pts, $F_i > (F_{\text{med}} - 4.5\sigma_i)^{\text{b}}$	93% pts, $F_i > (F_{\text{med}} - 8\sigma_i)^{\text{b}}$	<11 pts, $F_i < (F_{\text{med}} - 11\sigma_i)^{\text{b}}$
pulsating var.	<5 pts <sup>d</sup> , $F_i < (F_{\text{med}} - 3.5\sigma_i)^{\text{b}}$	< 4 pts <sup>d</sup> , $F_i < (F_{\text{med}} - 5.5\sigma_i)^{\text{b}}$	<5 pts <sup>d</sup> , $F_i < (F_{\text{med}} - 5.5\sigma_i)^{\text{c}}$
2nd peak	$SN_{p3} < 13\sigma_i$ , $t_i > (t_{\text{max}} + 110)^{\text{b}}$	$SN_{p4} < 16\sigma_i$ , $t_i > (t_{\text{max}} + 110)^{\text{c}}$	
photometry std	95% pts, $F_i < F_{\text{p}}^{\text{a}}$	> 100 good photometry pts <sup>a</sup>	

NOTE.—Microlensing event selection cuts. We denote the uncertainty in an individual flux measurement  $F_i$ , taken at time  $t_i$ , as  $\sigma_i$ . Event peaks occur with flux measurement  $F_{\text{p}}$  at  $\approx t_{\text{max}}$ . The median flux value for a lightcurve is  $F_{\text{med}}$ . The total signal to ratio of three points in a second peak is denoted  $SN_{p3}$ . For four points this is denoted  $SN_{p4}$ .

<sup>a</sup> In  $R_m$  or  $B_m$  bands.

<sup>b</sup> In  $R_m$  &  $B_m$  bands.

<sup>c</sup> In  $R_m$  band.

<sup>d</sup> Consecutive good photometry points.

TABLE 2  
PARAMETERS OF LEVEL-1.5 & 2.0 CUTS.

Level	$F_{\text{pr}}$	$A_{\text{F}(>)}$	$\chi_{c(<)}$	$\chi_{m(<)}$	$\text{SN}_{\text{r}(>)}$
1.5	...	1.34	9.3	3.0	...
1.5	$> 2.5\text{e}4$	1.34	15	...	...
1.5	$> 5\text{e}4$	1.34	30	...	...
1.5	$> 3\text{e}2$	10	9.5	4.0	...
1.5	$> 3\text{e}2$	20	15	4.0	...
1.5	$> 3\text{e}3$	20	15	...	...
1.5	$> 3\text{e}4$	10	30	...	100
2.0	$< 8\text{e}3$	1.34	...	$1.65 + 1.8\text{e-}4 F_{\text{pr}}$	...
2.0	$< 1\text{e}4$	1.34	$3.75 + 6.0\text{e-}4 F_{\text{pr}}$	...	...
2.0	$1\text{e}4 < F_{\text{pr}} < 1\text{e}5$	1.34	...	...	$2 + 2\text{e-}4 F_{\text{pr}}$
2.0	$> 1\text{e}4$	1.34	...	...	...

NOTE.—Microlensing event selection cuts. All level 1.5 events must pass the cuts in the text ( $V - R > 0.55$ ,  $A > 1.34$ ,  $\Omega\chi^2 < 3.6$ ,  $\hat{t} < 365$  days,  $t_{\text{max}_{ij}} \neq t_{\text{max}_{kj}}$ ,  $\chi_c^2 < 30$ ) in addition to one line of level 1.5 cuts. All events must also pass all 2.0 cuts for which their red fit peak flux  $F_{\text{pr}}$  is in the range of the cut. Unlisted values specify no cut is applied on that parameter. Here  $A_{\text{F}(>)}$  specifies that the fitted microlensing event amplitudes  $A_{\text{F}}$  must be greater to pass this cut. Likewise for the other columns, signal to noise ratio in the red band ( $\text{SN}_{\text{r}}$ ), microlensing fit reduced chi square  $\chi_m$  and constant baseline fit reduced chi square  $\chi_c$ .

TABLE 3  
INDIVIDUAL FIELDS.

Field	SOD	DIA	New	$l$ ( $^{\circ}$ )	$b$ ( $^{\circ}$ )	$r$	$p$ (%)	$\tau$ ( $10^6$ )
101	6	11	6	3.728	-3.021	1.12	11.8	$1.72^{+0.60}_{-0.48}$
104	10	16	10	3.109	-3.008	1.17	10.6	$4.18^{+1.62}_{-1.35}$
108	12	16	8	2.304	-2.649	1.43	11.4	$2.39^{+0.67}_{-0.57}$
113	9	17	9	1.629	-2.781	1.57	8.9	$1.96^{+0.54}_{-0.45}$
118	8	13	8	0.833	-3.074	1.41	10.0	$2.64^{+0.89}_{-0.78}$
119	6	12	7	1.065	-3.831	1.00	9.3	$2.43^{+0.86}_{-0.72}$
128	4	10	7	2.433	-4.029	0.91	8.4	$1.62^{+0.62}_{-0.47}$
159	3	4	2	6.353	-4.402	0.48	9.3	$1.06^{+0.84}_{-0.66}$

NOTE.— Col. (1), field number Id. Col. (2), number of events which pass cuts performed on SodoPhot photometry as of August 1999. Col. (3), number of events from the Difference Image Analysis. Col. (4), number of new events from this analysis. Cols. (5) & (6), field location. Col. (7), Number of clump stars relative to field 119 (BW). Col. (8), Percentage of disk stars in each field to  $V = 23$ . Col. (9), microlensing optical depth.

TABLE 4  
CANDIDATE MICROLENSING EVENTS.

Event Id	DIA Id	MACHO Id	RA (J2000)	Dec (J2000)	S (")
95-BLG-d6 <sup>v</sup>	101.14.1893	101.21688.5320	18 07 02.02	-27 32 40.2	1.47
95-BLG-30 <sup>f</sup>	101.15.3933	101.21821.128	18 07 04.27	-27 22 06.3	0.16
95-BLG-d7	101.15.3935	101.21950.1897	18 07 25.07	-27 24 41.1	1.28
95-BLG-s8	101.15.3936	101.21691.836	18 06 52.77	-27 23 19.8	0.55
96-BLG-d2	101.19.3670	101.21171.4799	18 05 38.12	-27 23 07.8	0.51
97-BLG-24	101.21.3714	101.20650.1216	18 04 20.26	-27 24 45.8	0.51
97-BLG-42	101.22.3422	101.20914.3873	18 04 56.56	-27 10 43.2	3.75
95-BLG-5	101.23.3319	101.20658.2639	18 04 22.40	-26 53 15.8	0.56
97-BLG-s4	101.24.2939	101.21174.3417	18 05 38.80	-27 08 29.5	1.06
96-BLG-d3	101.24.2940	101.21174.2131	18 05 47.03	-27 08 54.8	0.43
95-BLG-15	101.26.2507	101.21564.4657	18 06 28.79	-27 09 35.9	0.85
95-BLG-s9	104.14.5859	104.21161.1997	18 05 34.46	-28 02 51.7	0.24
96-BLG-d4	104.15.7362	104.21162.3642	18 05 47.75	-27 56 32.9	0.01
96-BLG-d5	104.15.7365	104.21423.530	18 06 09.00	-27 53 39.1	1.42
96-BLG-d6	104.15.7366	104.21033.4316	18 05 29.53	-27 54 00.6	2.38
96-BLG-14	104.16.4493	104.21032.4118	18 05 15.39	-27 58 24.4	0.71
97-BLG-d5	104.16.4494	104.20901.1319	18 05 02.68	-28 00 47.7	0.56
96-BLG-12 <sup>p</sup>	104.19.5184	104.20382.803	18 03 53.20	-27 57 35.7	0.14
96-BLG-1	104.19.5185	104.20645.3129	18 04 26.19	-27 47 35.0	0.25
97-BLG-38	104.19.5186	104.20514.1500	18 04 06.10	-27 48 26.9	0.72
95-BLG-d10	104.19.5187	104.20643.299	18 04 25.12	-27 54 31.6	0.93
97-BLG-18	104.20.5880	104.20121.1692	18 03 15.26	-28 00 13.9	0.13
97-BLG-58	104.24.4584	104.20515.498	18 04 09.68	-27 44 35.1	0.27
95-BLG-d11	104.24.4585	104.20517.707	18 04 06.15	-27 39 21.4	0.21
96-BLG-26	104.25.4571	104.20388.2766	18 03 53.97	-27 33 30.5	0.08
97-BLG-2	104.26.4393	104.20775.2644	18 04 50.73	-27 45 57.3	0.09
96-BLG-d7 <sup>b</sup>	104.27.4089	101.20908.1433	18 04 57.73	-27 33 18.3	0.71
97-BLG-d6 <sup>v</sup>	113.14.6365	113.19454.768	18 01 35.64	-29 08 39.3	0.87
95-BLG-d12	113.14.6367	113.19322.2128	18 01 15.47	-29 18 06.6	1.33
95-BLG-s13	113.16.6650	113.18934.4131	18 00 28.87	-29 09 34.9	0.63
96-BLG-d8	113.16.6651	113.19192.228	18 01 04.67	-29 17 31.1	0.52
96-BLG-d9	113.16.6652	113.18932.3227	18 00 26.34	-29 17 36.1	3.01
97-BLG-1 <sup>b</sup>	113.18.6227	113.18674.756	17 59 53.38	-29 09 07.8	0.47
95-BLG-4	113.18.6228	113.18804.1061	18 00 03.41	-29 11 04.3	0.73
96-BLG-21	113.21.5667	113.18156.1823	17 58 43.15	-29 00 30.0	1.83
97-BLG-d7 <sup>b</sup>	113.21.5669	113.18286.536	17 59 02.71	-29 03 02.5	0.24
96-BLG-s10	113.22.6004	113.18420.5494	17 59 25.01	-28 46 32.9	0.61
95-BLG-1	113.23.5372	113.18292.2374	17 59 00.57	-28 36 57.3	0.53
96-BLG-20	113.24.6037	113.18550.1664	17 59 40.59	-28 47 24.9	0.53
96-BLG-10	113.25.5974	113.18680.3511	18 00 02.01	-28 45 17.6	0.68
95-BLG-23	113.25.5975	113.18812.4511	18 00 03.61	-28 39 14.8	1.15
97-BLG-d8	113.26.5353	113.18938.3003	18 00 32.48	-28 53 22.7	0.83
95-BLG-d14	113.26.5354	113.18940.3399	18 00 34.56	-28 47 06.5	2.35
95-BLG-d15	113.26.5357	113.19070.2853	18 00 46.72	-28 46 45.0	0.79
96-BLG-8	118.15.7509	118.19184.3770	18 00 58.17	-29 49 50.5	0.50
96-BLG-d11	118.17.3390	118.18663.1884	18 00 01.63	-29 52 19.7	0.76
97-BLG-16	118.17.6294	118.18662.2180	17 59 56.37	-29 56 37.5	0.70
97-BLG-4	118.18.5693	118.18270.3615	17 59 04.71	-30 07 06.5	0.90
96-BLG-d12	118.18.6885	118.18531.1816	17 59 37.67	-30 00 53.1	0.53
97-BLG-8 <sup>p</sup>	118.18.6886	118.18529.538	17 59 35.35	-30 08 48.1	0.36
95-BLG-d16	118.19.7905	118.18404.992	17 59 18.58	-29 47 49.4	0.52
95-BLG-d17 <sup>v</sup>	118.20.1711	118.19050.2888	18 00 42.46	-30 06 37.2	2.16
96-BLG-d12	118.21.3144	118.18143.4794	17 58 34.55	-29 53 13.4	2.98
97-BLG-d9	118.23.7346	118.18019.3386	17 58 28.69	-29 29 11.5	1.44
95-BLG-10	118.23.7347	118.18018.2379	17 58 16.01	-29 32 10.9	0.06
96-BLG-d13	118.25.5470	118.18539.3614	17 59 34.95	-29 30 04.2	0.86
97-BLG-26 <sup>p</sup>	118.26.5695	118.18797.1397	18 00 06.94	-29 38 06.0	0.01

TABLE 4—*Continued*

Event Id	DIA Id	MACHO Id	RA (J2000)	Dec (J2000)	S (")
97-BLG-d10	119.14.4347	119.20479.459	18 04 13.52	-30 09 25.9	0.16
95-BLG-11	119.14.4348	119.20738.3418	18 04 37.26	-30 12 11.6	0.41
97-BLG-14	119.15.5936	119.20480.2914	18 04 16.36	-30 07 23.2	0.18
97-BLG-37	119.17.5482	119.20352.2589	18 03 58.66	-29 58 48.8	0.08
95-OGLE-16	119.21.1551	119.19571.1616	18 02 07.62	-30 01 12.7	0.46
96-BLG-3 <sup>b</sup>	119.22.1686	119.19444.2055	18 01 45.54	-29 49 47.1	0.28
95-BLG-d18	119.22.4857	119.19704.1819	18 02 22.70	-29 50 35.2	0.74
95-BLG-39	119.23.4960	119.19576.2024	18 02 04.76	-29 43 15.6	0.27
95-BLG-d19	119.23.541	119.19447.724	18 01 41.23	-29 37 23.2	0.47
95-BLG-d20	119.25.1896	119.20096.2073	18 03 07.84	-29 40 09.7	1.04
95-BLG-3	119.25.5509	119.19837.1072	18 02 37.52	-29 39 35.9	0.12
97-BLG-d11	119.26.5056	119.20223.2492	18 03 33.85	-29 53 30.0	2.73
96-BLG-d14	128.15.5153	110.22318.4078	18 08 24.14	-28 54 59.9	2.21
96-BLG-d15	128.16.4751	128.21923.1479	18 07 32.70	-29 13 06.8	2.81
96-BLG-s16	128.17.5429	128.22057.2384	18 07 38.96	-28 57 11.8	0.05
96-BLG-d17	128.20.3810	128.21145.1300	18 05 40.51	-29 05 59.6	1.12
96-BLG-d18	128.22.4279	128.21410.1924	18 06 07.41	-28 47 25.5	0.25
95-BLG-d21	128.23.4933	128.21153.867	18 05 36.73	-28 32 41.5	0.08
96-BLG-31	128.24.4809	128.21541.1133	18 06 42.39	-28 41 15.9	0.12
97-BLG-d12	128.24.4810	128.21671.4941	18 06 52.95	-28 42 19.2	2.87
95-BLG-d22	128.26.4587	128.21800.522	18 07 11.15	-28 46 59.8	0.89
95-BLG-18 <sup>p</sup>	128.27.4562	128.21932.1362	18 07 20.56	-28 36 51.1	0.57
97-BLG-d13	159.14.3680	159.26652.168	18 18 21.08	-25 56 37.1	0.43
95-BLG-22	159.16.3693	159.26132.3182	18 17 14.80	-25 55 58.2	0.20
97-BLG-s14	159.21.3328	159.25486.1627	18 15 42.76	-25 41 01.9	1.34
97-BLG-d15 <sup>v</sup>	159.25.4026	177.26012.459	18 16 51.10	-25 19 03.8	1.10

NOTE.—Col. (1) gives the event ID. Col. (2) gives the ID for DIA light curve. Col. (3) gives the identification number of the nearest monitored SoDoPhot object. Cols. (4) & (5) are the centroid location coordinates of the event. Col. (6), the separation  $S$  of the event centroid from the SoDoPhot object centroid. We have not included events from field 108 as these have been presented in Alcock et al. (1999c). Events where the centroid offset  $S$  is  $> 1$  pixel from any SoDoPhot object are likely Pixel lensing events.

<sup>f</sup> Finite source event

<sup>b</sup> Binary lens event

<sup>p</sup> Parallax event

<sup>v</sup> Possible variable

TABLE 5  
PARAMETERS OF CLASSICAL MICROLENSING EVENTS.

Event Id	$\hat{t}_{ns}$ (days)	$\hat{t}_s$ (days)	$t_{max}$	$A_{ns}$	$A_s$	$V_{ns}$	$V_s$	$(V - R)_{ns}$	$(V - R)_s$
95-BLG-30	$60.62 \pm 0.03$	$72.2 \pm 0.3$	$1321.38 \pm 0.01$	14.06	24.77	16.27	$16.59^{+0.01}_{-0.01}$	1.37	1.39
95-BLG-s8	$28.6 \pm 0.2$	$41.9 \pm 1.8$	$836.14 \pm 0.06$	1.76	2.94	17.17	$18.37^{+0.11}_{-0.10}$	0.55	0.72
97-BLG-24	$9.7 \pm 0.2$	$25.4 \pm 4.5$	$1594.29 \pm 0.11$	2.99	42.80	17.98	$20.00^{+0.34}_{-0.26}$	0.59	0.64
95-BLG-5	$17.7 \pm 0.4$	$17.6 \pm 2.7$	$827.90 \pm 0.06$	6.80	6.73	20.71	$20.62^{+0.29}_{-0.23}$	0.91	0.84
95-BLG-s9	$30.4 \pm 0.2$	$41.0 \pm 1.4$	$925.21 \pm 0.02$	5.99	8.77	18.63	$19.10^{+0.05}_{-0.05}$	0.74	0.74
97-BLG-d5	$59.1 \pm 2.3$	$111.3 \pm 21.8$	$1527.99 \pm 0.89$	1.36	3.09	18.20	$19.96^{+0.54}_{-0.36}$	0.76	0.72
96-BLG-12	$236.7 \pm 0.9$	$297.9 \pm 11.0$	$1399.31 \pm 0.32$	16.46	70.65	17.77	$18.19^{+0.09}_{-0.08}$	0.89	0.86
96-BLG-1	$147.4 \pm 1.3$	$158.2 \pm 10.0$	$1180.88 \pm 0.42$	1.69	1.83	17.70	$17.89^{+0.20}_{-0.17}$	1.04	1.03
97-BLG-18	$140.7 \pm 0.9$	$161.1 \pm 11.4$	$1609.24 \pm 0.20$	2.14	2.56	18.57	$18.96^{+0.17}_{-0.15}$	0.82	0.88
97-BLG-58	$52.2 \pm 5.5$	$61.9 \pm 278.5$	$1683.67 \pm 7.40$	1.64	2.19	17.63	$18.42^{+0.20}_{-3.39}$ <sup>a</sup>	0.93	0.90
95-BLG-d11	$111.7 \pm 21.4$	$124.8 \pm 632.2$	$715.01 \pm 41.88$	1.51	1.54	17.34	$18.35^{+0.45}_{-3.45}$	0.85	0.97
96-BLG-26	$55.4 \pm 0.7$	$105.1 \pm 8.3$	$1315.03 \pm 0.08$	5.03	11.15	19.83	$20.54^{+0.12}_{-0.11}$	0.90	0.56
97-BLG-2	$38.8 \pm 0.7$	$55.4 \pm 6.9$	$1523.27 \pm 0.07$	4.61	7.14	20.03	$20.29^{+0.21}_{-0.17}$	0.86	0.64
97-BLG-1	$76.0 \pm 0.2$	$44.6 \pm 0.9$	$1511.65 \pm 0.03$	4.76	2.18	17.39	$16.05^{+0.06}_{-0.06}$	0.90	0.84
97-BLG-d7	$14.7 \pm 0.2$	$22.1 \pm 3.5$	$1618.44 \pm 0.14$	1.14	1.45	17.04	$18.21^{+0.72}_{-0.43}$	0.83	0.74
95-BLG-1	$40.6 \pm 0.2$	$57.5 \pm 2.8$	$816.80 \pm 0.03$	8.56	13.13	19.16	$19.61^{+0.07}_{-0.07}$	1.00	0.94
96-BLG-20	$40.6 \pm 0.6$	$61.0 \pm 6.0$	$1273.57 \pm 0.26$	1.83	3.21	18.43	$19.33^{+0.25}_{-0.20}$	0.89	0.69
97-BLG-8	$98.2 \pm 0.2$	$159.9 \pm 2.1$	$1575.50 \pm 0.01$	17.24	31.48	19.53	$20.18^{+0.02}_{-0.02}$	1.02	1.02
95-BLG-d16	$8.1 \pm 0.6$	$18.1 \pm 12.6$	$896.33 \pm 0.40$	1.26	4.16	18.23	$20.94^{+0.16}_{-0.89}$	0.85	0.72
95-BLG-10	$79.3 \pm 0.7$	$89.3 \pm 5.8$	$869.15 \pm 0.17$	2.31	2.71	19.04	$19.29^{+0.16}_{-0.14}$	0.77	0.70
97-BLG-26	$111.4 \pm 0.2$	$127.7 \pm 1.9$	$1636.63 \pm 0.02$	7.05	8.38	19.38	$19.47^{+0.02}_{-0.02}$	1.26	1.16
97-BLG-d10	$70.0 \pm 0.6$	$87.2 \pm 7.8$	$1636.49 \pm 0.24$	1.22	1.45	16.91	$17.73^{+0.34}_{-0.26}$	0.73	0.75
95-BLG-11	$22.5 \pm 0.2$	$31.2 \pm 1.9$	$853.36 \pm 0.02$	22.89	33.02	20.04	$20.58^{+0.09}_{-0.08}$	0.90	0.98
97-BLG-14	$47.4 \pm 1.4$	$60.6 \pm 12.1$	$1561.32 \pm 0.36$	1.83	2.40	19.72	$20.37^{+0.66}_{-0.41}$	0.79	0.91
97-BLG-37	$21.6 \pm 0.3$	$103.9 \pm 9.7$	$1610.86 \pm 0.08$	1.74	13.88	17.48	$20.62^{+0.14}_{-0.12}$	0.54	0.69
95-OGLE-16	... <sup>b</sup>	$41.8 \pm 26.3$	$884.38 \pm 0.68$	...	1.35	...	$19.45^{+0.20}_{-0.20}$	...	0.89
96-BLG-3	$46.4 \pm 0.2$	$71.7 \pm 3.8$	$1167.33 \pm 0.02$	14.38	24.48	19.15	$19.85^{+0.07}_{-0.07}$	0.70	0.81
95-BLG-39	$39.3 \pm 0.7$	$53.5 \pm 5.2$	$993.97 \pm 0.19$	2.21	3.66	18.77	$19.51^{+0.22}_{-0.19}$	0.65	0.53
95-BLG-d19	$55.7 \pm 1.6$	$104.2 \pm 31.7$	$936.83 \pm 0.82$	1.15	1.98	17.92	$19.84^{+1.51}_{-0.61}$	0.75	0.53
95-BLG-3	$2.28 \pm 0.04$	$2.9 \pm 0.6$	$809.29 \pm 0.02$	4.80	7.05	18.93	$19.47^{+0.52}_{-0.35}$	1.01	1.05
96-BLG-s16	$74.8 \pm 2.2$	$73.3 \pm 18.0$	$1339.17 \pm 0.77$	1.55	1.51	19.12	$19.09^{+1.43}_{-0.60}$	0.51	0.56
96-BLG-d18	$5.4 \pm 0.2$	$6.5 \pm 2.7$	$1255.38 \pm 0.07$	1.69	2.11	19.11	$19.62^{+0.77}_{-0.77}$	0.82	0.63
95-BLG-d21	$31.8 \pm 0.6$	$35.6 \pm 9.8$	$872.37 \pm 0.29$	1.32	1.46	18.02	$18.35^{+1.87}_{-0.65}$	0.85	0.79
96-BLG-31	$49.6 \pm 0.4$	$54.4 \pm 1.8$	$1373.14 \pm 0.05$	4.80	6.09	18.80	$18.88^{+0.08}_{-0.07}$	0.92	0.80
95-BLG-18	$83.1 \pm 0.9$	$98.7 \pm 10.1$	$904.18 \pm 0.29$	1.70	2.18	18.93	$19.55^{+0.31}_{-0.24}$	0.79	0.93
97-BLG-d13	$5.82 \pm 0.09$	$25.7 \pm 3.2$	$1607.01 \pm 0.05$	1.13	6.39	16.75	$20.65^{+0.23}_{-0.19}$	0.74	0.70
95-BLG-22	$19.9 \pm 0.7$	$20.1 \pm 4.3$	$899.82 \pm 0.13$	4.97	4.85	20.75	$20.80^{+0.54}_{-0.36}$	0.70	0.79

NOTE.—The results of two types of fits. One where the source flux is assumed to be that of the nearest SoDoPhot source. The other where the source flux is also used as a fit parameter. The parameters from the fits are denoted by the subscripts *ns* (no source fit) and *s* (source fit) respectively. We have not include events from field 108 as these have been presented in Alcock et al. (1999c). Col. (1), the DIA light curve identification number. Cols. (2) & (3), the fit timescale of the event. Col. (4), the time of maximum amplification (JD  $-2449000$ ). Cols (5) & (6), the amplifications of these two fits. Col. (7), the baseline magnitude of the SoDoPhot object. Col. (8), the fitted source magnitude. Col. (9), the colour of the nearest SoDoPhot object. Col. (10), the fit colour of the object. In all cases the presented uncertainties are the formal  $1\sigma$  errors from the fitting process.

<sup>a</sup> Events where a lower limit to the source flux was not determined.

<sup>b</sup> Nearest SoDoPhot source has  $R_m$  band data only.

TABLE 6  
PARAMETERS OF PIXEL MICROLENSING EVENTS.

Event Id	$\hat{t}$ (days)	$t_{max}$	A	$V_{fit}$	$(V-R)_{fit}$
95-BLG-d6	$9.5 \pm 13.8$	$873.46 \pm 0.60$	1.73	$20.56_{-1.76}^{+0.93}$	0.56
95-BLG-d7	$34.4 \pm 16.8$	$872.24 \pm 0.06$	17.36	$22.59_{-0.49}^{+0.93}$	0.91
96-BLG-d2	$30.0 \pm 11.9$	$1222.84 \pm 0.23$	3.99	$21.51_{-0.57}^{+1.25}$	1.02
97-BLG-42	$37.5 \pm 12.5$	$1635.06 \pm 0.34$	2.21	$20.41_{-0.63}^{+1.67}$	0.67
97-BLG-s4	$25.8 \pm 5.2$	$1533.26 \pm 0.15$	7.68	$20.21_{-0.30}^{+0.42}$	0.73
96-BLG-d3	$107.7 \pm 14.6$	$1172.75 \pm 0.09$	19.03	$21.20_{-0.18}^{+0.21}$	0.57
95-BLG-15	$37.6 \pm 4.0$	$853.84 \pm 0.04$	22.80	$21.16_{-0.14}^{+0.16}$	0.67
96-BLG-d4	$202.5 \pm 72.2$	$1319.32 \pm 0.78$	9.66	$22.10_{-0.43}^{+0.73}$	0.82
96-BLG-d5	$62.6 \pm 15.8$	$1258.99 \pm 0.39$	4.04	$21.15_{-0.40}^{+0.64}$	0.85
96-BLG-d6	$10.0 \pm 2.2$	$1247.00 \pm 0.03$	49.41	$21.43_{-0.27}^{+0.36}$	0.83
96-BLG-14	$37.9 \pm 6.7$	$1244.09 \pm 0.17$	3.26	$20.13_{-0.32}^{+0.46}$	0.68
97-BLG-38	$12.2 \pm 3.3$	$1616.52 \pm 0.01$	33.85	$21.13_{-0.35}^{+0.51}$	0.86
95-BLG-d10	$84.7 \pm 7.1$	$866.39 \pm 0.08$	10.93	$20.45_{-0.12}^{+0.13}$	0.73
96-BLG-d7	$18.9 \pm 10.2$	$1221.76 \pm 0.25$	2.12	$20.22_{-0.88}^{+0.92}$	0.86
97-BLG-d6	$12.4 \pm 13.0$	$1632.81 \pm 0.39$	1.58	$19.96_{-1.51}^{+0.92}$	0.58
95-BLG-d12	$91.4 \pm 23.5$	$804.21 \pm 0.90$	2.58	$20.15_{-0.49}^{+0.92}$	0.96
95-BLG-s13	$25.0 \pm 15.2$	$806.19 \pm 0.14$	87.45	$22.25_{-0.67}^{+2.11}$	0.96
96-BLG-d8	$31.4 \pm 3.6$	$1225.88 \pm 0.02$	50.90	$22.51_{-0.13}^{+0.15}$	1.32
96-BLG-d9	$10.3 \pm 3.9$	$895.32 \pm 0.02$	18.94	$22.07_{-0.39}^{+0.62}$	0.94
95-BLG-4	$13.7 \pm 7.3$	$790.09 \pm 0.10$	4.44	$20.31_{-0.66}^{+1.97}$	0.91
96-BLG-21	$41.9 \pm 7.2$	$1272.15 \pm 0.14$	6.56	$20.96_{-0.25}^{+0.33}$	0.78
96-BLG-s10	$35.5 \pm 4.3$	$1169.70 \pm 0.03$	9.80	$20.40_{-0.16}^{+0.19}$	0.59
96-BLG-10	$62.0 \pm 7.7$	$1236.97 \pm 0.07$	10.92	$21.05_{-0.18}^{+0.21}$	0.81
95-BLG-23	$21.1 \pm 7.8$	$900.93 \pm 0.25$	4.03	$21.15_{-0.56}^{+1.24}$	0.83
97-BLG-d8	$18.0 \pm 8.7$	$1525.98 \pm 0.21$	3.51	$20.87_{-0.70}^{+2.61}$	0.86
95-BLG-d14	$24.5 \pm 3.4$	$816.36 \pm 0.04$	11.70	$20.10_{-0.20}^{+0.24}$	0.71
95-BLG-d15	$47.6 \pm 10.0$	$886.35 \pm 0.35$	1.90	$19.44_{-0.46}^{+0.81}$	0.77
96-BLG-8	$39.7 \pm 9.8$	$1224.63 \pm 0.05$	20.82	$22.24_{-0.29}^{+0.39}$	1.00
96-BLG-d11	$49.3 \pm 28.1$	$1249.74 \pm 0.38$	5.98	$22.50_{-0.67}^{+2.15}$	0.79
97-BLG-16	$38.3 \pm 8.6$	$1567.20 \pm 0.30$	3.13	$21.05_{-0.41}^{+0.67}$	1.12
97-BLG-4	$25.4 \pm 9.0$	$1518.15 \pm 0.04$	51.38	$22.62_{-0.37}^{+0.56}$	0.97
96-BLG-d12	$171.0 \pm 65.4$	$1183.51 \pm 1.29$	4.42	$21.92_{-0.55}^{+1.17}$	0.64
95-BLG-d17	$12.0 \pm 13.3$	$853.74 \pm 0.50$	1.40	$18.67_{-1.66}^{+0.67}$	0.72
96-BLG-d12	$27.8 \pm 13.1$	$1250.07 \pm 0.19$	5.69	$21.78_{-0.59}^{+1.38}$	0.62
97-BLG-d9	$90.1 \pm 32.3$	$1546.12 \pm 0.30$	10.96	$22.84_{-0.44}^{+0.75}$	0.86
96-BLG-d13	$33.5 \pm 10.1$	$1317.54 \pm 0.15$	7.94	$21.71_{-0.39}^{+0.62}$	0.87



TABLE 6—*Continued*

Event Id	$\hat{t}$ (days)	$t_{max}$	A	$V_{fit}$	$(V-R)_{fit}$
95-BLG-d18	$20.2 \pm 13.1$	$954.71 \pm 0.24$	4.12	$21.75_{-0.83}^{...}$	0.65
95-BLG-d20	$26.7 \pm 4.7$	$869.10 \pm 0.06$	12.31	$20.76_{-0.23}^{+0.30}$	0.75
97-BLG-d11	$49.3 \pm 10.1$	$1607.01 \pm 0.31$	2.90	$20.13_{-0.38}^{+0.60}$	0.63
96-BLG-d14	$93.5 \pm 15.7$	$1140.66 \pm 12.00$	14.31	$19.43_{-0.63}^{+1.70}$	0.82
96-BLG-d15	$26.3 \pm 6.1$	$1332.95 \pm 0.06$	12.74	$21.57_{-0.32}^{+0.46}$	0.81
96-BLG-d17	$42.5 \pm 7.3$	$1257.79 \pm 0.23$	2.70	$19.73_{-0.34}^{+0.49}$	0.93
97-BLG-d12	$11.5 \pm 6.3$	$1630.10 \pm 0.11$	4.47	$21.72_{-0.71}^{+2.75}$	0.74
95-BLG-d22	$24.5 \pm 5.3$	$938.76 \pm 0.04$	19.08	$21.12_{-0.29}^{+0.40}$	0.62
97-BLG-s14	$134.8 \pm 16.9$	$1633.64 \pm 0.19$	6.71	$21.48_{-0.18}^{+0.22}$	0.73
97-BLG-d15	$27.7 \pm 19.4$	$1569.43 \pm 0.65$	2.84	$21.41_{-1.00}^{...}$	0.68

NOTE.—Events where offset  $> 1$  pixel from any SoDoPhot object or the fitted baseline magnitude is below the detection threshold for SoDoPhot. Parameters come from fits to the DIA photometry light curves. In all cases the presented uncertainties are the formal  $1\sigma$  errors from the fitting process. Values of  $t_{max}$  are (JD  $-2449000$ ). Events for field 108 have been presented in Alcock et al. (1999c).

<sup>a</sup> Events where a lower limit to the source flux was not determined.

TABLE 7  
MEASUREMENTS OF BAR ORIENTATION.

Ref	Method	Inclination Angle ( $\theta$ )
1	Gas Dynamics ( $H_I$ )	30–45
2	Gas Dynamics ( $H_I, CO, CS$ )	$16 \pm 2$
3	Main Sequence Star CMD	$18 \pm 3$
4	Dirbe non-parametric deprojection	10–40
5	2-D Gas Simulations ( $H_I, CO$ )	$> 25$
6	Dirbe L,M-band deprojection	15–35
7	COBE K-band constrained N-Body Sim	$28 \pm 8$
8	Star Counts	$19 \pm 1$
8	Star Counts	$24 \pm 2$
9	Red-clump giant numbers	10–45
10	OGLE+MACHO Microlensing	$< 30$
11	Fux N-body & OH/IR stars	$44 \pm \sim 5$
12	2-D simulations & $H_I$ data	$35 \pm 5$

REFERENCES.— (1) de Vaucouleurs 1964; (2) Binney et al. 1991; (3) Bertelli et al. 1995; (4) Dwek et al. 1995; (5) Weiner 1996; (6) Binney, Gerhard, & Spergel 1997; (7) Fux 1997; (8) Nikolaev & Weinberg 1997; (9) Stanek et al. 1997; (10) Gyuk 1999; (11) Sevenster et al. 1999; (12) Weiner & Sellwood 1999

NOTE.—Col. (1), reference. Col. (2), the observation or method used in determination. Col. (3), the bar inclination angle relative to Sun-GC line-of-sight with uncertainties if given.

TABLE 8  
OPTICAL DEPTHS FROM MODELS

Ref	Model	$M_b(10^{10}M_\odot)$	$\tau (10^{-6})$
1	double exp disk	...	0.4–0.8
2	double exp disk + halo	...	0.5–1.1
3	symetric bulge + massive disk	1.9	1.9
4	bar + truncated disk	2.0	$2.2 \pm 0.45$
5	bar + double exp disk	1.8	1.9
6	N-body model (m08t3200)	3.0 <sup>a</sup>	1.8
6	N-body model (m04t3000)	5.0 <sup>a</sup>	2.0
7	non-bisymmetric disk	1.65	1.1–1.8
7	bisymmetric disk	1.65	1.1–1.6
8	bar + nucleus + dble exp disk	2.2	1.54
8	bar + nucleus + dble exp disk	3.3	2.14
9	Fux N-body & OH/IR stars	2.0	2.2
10	maximum likelihood	...	$1.93 \pm 0.39$
11	thick & thin disk	1.8	1.9
12	Schwarzschild orbits	...	1.4

REFERENCES.— (1) Paczyński 1991; (2) Griest et al. 1991; (3) Evans 1994; (4) Zhao, Spiegel, & Rich 1995; (5) Alcock et al. 1997b; (6) Fux 1997 (7) Nikolaev & Weinberg 1997; (8) Peale 1998; (9) Sevenster et al. 1999; (10) Gyuk 1999; (11) Grenacher et al. 1999; (12) Hafner et al. 1999.

NOTE.—Col. (1), reference. Col. (2), characteristic feature of model. Col. (3), Bulge/Bar mass used in model (if known). Col. (4), optical depth obtain from model.

<sup>a</sup> Spheroid plus nucleus mass